

He-atom-scattering studies of the structure and dynamics of the $\text{KMnF}_3(001)$ surface and the 186-K phase transition

J. P. Toennies and R. Vollmer

Max-Planck-Institut für Strömungsforschung, Bunsenstrasse 10, Göttingen, Germany

(Received 6 May 1991)

A phase transition at the surface of $\text{KMnF}_3(001)$ is observed by helium-atom-scattering diffraction and surface-phonon-dispersion-curve measurements at $T_c^s = 191$ K. This transition temperature is only slightly above the corresponding bulk phase transition at $T_c^b = 187.5$ K. As in the bulk, the phase transition is found to be weakly first order and is driven by the softening of the Rayleigh mode at the \bar{M} point. Critical scattering is observed up to 320 K. At temperatures higher than ≈ 420 K an irreversible change in the diffraction intensity is observed, indicating a transition to a partially disordered surface.

I. INTRODUCTION

Many perovskites exhibit bulk structural phase transitions driven by the softening of a phonon mode. During the past 20 years neutron scattering and x-ray scattering as well as other methods such as ESR, NMR, Mössbauer, and light scattering reported in the reviews of Cowley¹ and Müller² have been extensively employed to study the phenomena accompanying these phase transitions. On cooling below room temperature KMnF_3 undergoes two structural phase transitions, both accompanied by the softening of a particular phonon mode. In the early neutron experiments of Shirane *et al.*³ the first transition was observed to occur at $T_c^b \approx 186$ K due to the softening of the Γ_{25} mode at the R point, which is the zone boundary in the $\langle 111 \rangle$ direction. The second transition was found at ≈ 90 K due to the softening of the M_3 mode, which is at the zone boundary in the $\langle 110 \rangle$ direction.³ Slightly differing values of the transition temperatures have since been reported in the literature. A more recent paper of Nicholls and Cowley⁴ reports $T_c^b = 187.5$ K. In early studies the second transition was reported to be at 91.5 K,^{3,5} whereas in a more recent paper Hidaka *et al.*⁶ found it at 88 K.

The bulk phase transition at $T_c^b \approx 186$ K is weakly first order, as indicated by a sudden jump in the diffraction intensity at the position of the superstructure peak of the low temperature phase.³ After this initial jump, however, the intensity increases strongly over a wide range of decreasing temperatures. Above the phase transition a strong softening of the Γ_{25} mode is observed and the low temperature phase has the displacement pattern of this mode.⁷ Thus, aside from the small initial jump in the diffraction peak intensity the overall behavior is more typical of a second-order phase transition. At the 90-K phase transition a softening of a phonon mode also occurs, but the diffracted intensity of the corresponding superstructure peak jumps immediately to its final value indicating a strong first-order phase transition.³

Starting at about 50 K above the 186-K phase transition an elastic component is observed in neutron scatter-

ing experiments. This peak critically diverges in intensity as the temperature approaches T_c^b from above.⁷ It was found that the width of this "central peak" is extremely small. For SrTiO_3 , which is very similar to KMnF_3 , the neutron backscattering experiments by Töpler *et al.*⁸ gave an upper limit of $0.08 \mu\text{eV}$, whereas in a Mössbauer γ -ray experiment the upper limit is reported to be $0.015 \mu\text{eV}$.⁹ Similar investigations on KMnF_3 are more difficult because of the first-order character of the phase transition and the strongly overdamped soft phonon close to the phase transition temperature whereas in SrTiO_3 the phase transition is pure second order. Presently, there exist mainly three different theories to explain this "central peak." The first group of theories attempts to explain the central peak through an anharmonic phonon perturbation theory¹⁰ but fails to explain the extraordinarily small energy width of the central peak. In the other theories the existence of two different time scales is assumed, a short-time scale of small vibrations around the equilibrium positions of the ions corresponding to the overdamped soft phonon, which occurs near the phase transition, and a long-time scale associated with the dynamics of precursor clusters having locally the symmetry of the low temperature phase. In the second set of theories the central peak is attributed to the cluster dynamics of a perfect crystal,¹¹ whereas in the third set of theories the presence of symmetry-breaking defects stabilizes the clusters resulting in a narrowing of the central peak.¹² Only the latter theory can explain the extremely small energy width of the central component in SrTiO_3 and KMnF_3 . In addition, the cluster formation induces a second length scale into the system in addition to the soft phonon correlation length. In x-ray experiments this second length scale is observable as a sharp peak at the superstructure peak position a few degrees above T_c^b superimposed on the broader soft phonon induced peak.^{4,13} A recent paper of Gibaud *et al.*¹⁴ demonstrates that the central component observed in the neutron spectra and the sharp peaks observed in the x-ray experiments have the same origin despite the different temperature range at which they are observed.

Compared to the bulk only little is known about the surface structure and dynamics of perovskite crystals. Figure 1 shows the structure of the unit cell of the KMnF_3 crystal. Also shown are the two possible surfaces which are produced when the crystal is cleaved in the (001) plane. One surface designated I or KF surface contains only K and F ions while the other surface II (MnF_2 surface) contains the Mn ions as well as F ions. The surface Brillouin zone and the irreducible part of it are shown in Fig. 1(c).

Recently the relaxation of the interlayer distance of $\text{SrTiO}_3(001)$ has been measured by low electron energy diffraction (LEED).¹⁵ The results agree well with the shell model calculations of Prade *et al.*¹⁶ The latter authors have also investigated theoretically the surface relaxation and dynamics of several perovskite surfaces including $\text{KMnF}_3(001)$ for which a surface soft phonon mode was predicted at the \bar{M} point.¹⁷ It was suggested that the phase transition associated with the softening of

this mode is at somewhat higher temperatures than the bulk transition.¹⁸ The influence of the surface termination and the possibility of a different transition temperature at the surface were previously discussed by Darlington and O'Connor⁹ who have measured a marked dependence of the central peak intensity upon the x-ray energy for SrTiO_3 . This was interpreted by assuming the existence of a thin surface layer which reconstructs at higher temperatures than the rest of the bulk and grows in thickness as the bulk transition temperature is approached. We will show in this paper that the $\text{KMnF}_3(001)$ surface reconstructs at only slightly higher temperatures than the bulk.

In the present experiments we have applied the method of helium scattering (HAS) to a study of the structure and dynamics of the $\text{KMnF}_3(001)$ surface over a wide range of temperatures from 125 K to ≈ 500 K. Compared to the more widespread methods of electron scattering HAS has the advantage that it is entirely non-destructive, an important consideration in view of the sensitivity of ionic crystals to electron stimulated desorption of ions from the surface. Moreover as demonstrated in the past HAS can be used for diffraction studies as well as high resolution measurements of surface phonon dispersion relations on all surfaces whereas the electron inelastic scattering (EELS) is difficult to apply to insulators and many semiconductors.^{19,20} Finally HAS has the advantage over other surface techniques in that it is uniquely sensitive to surface defects.²¹

This paper is organized as follows. After a short description of the experimental setup we report the results on the determination of the surface phase transition temperature. In Sec. III we present the results of the intensity behavior of the superstructure peaks below the surface phase transition temperature and the critical scattering above that temperature. The surface dynamics of KMnF_3 above and below the phase transition as well as the temperature dependence of the soft mode is discussed in Sec. IV. Finally evidence for the instability of the $\text{KMnF}_3(001)$ surface at temperatures above ≈ 420 K is presented in Sec. V. A summary and conclusions follow in Sec. VI.

II. EXPERIMENTAL

The helium atom scattering apparatus is similar to that described in Ref. 22. A highly monoenergetic beam is produced by a supersonic expansion of helium gas from a pressure of 40 to 450 bar, depending on the nozzle temperature, through a 10- μm nozzle into the vacuum resulting in a relative FWHM velocity spread of the beam of $\approx 0.5\%$. With a closed cycle refrigerator and a computer controlled resistive heater the temperature of the nozzle can be varied from ≈ 35 K to ≈ 350 K corresponding to kinetic energies of the helium atoms from ≈ 8 meV to ≈ 80 meV. After scattering from the crystal surface the helium atoms are detected at the end of a 142.8-cm-long flight tube by a sensitive homemade magnetic mass spectrometer. The angle between the incident beam and the scattered beam is fixed at 90° and the incident and final angles of the helium beam with respect to the surface

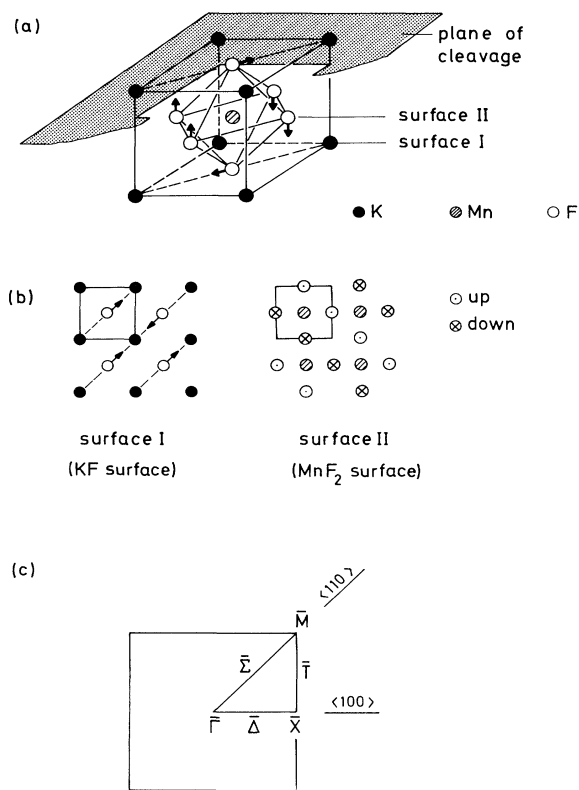


FIG. 1. (a) KMnF_3 unit cell and (001) plane of cleavage (b) structure of the two different possible cleavage surfaces. The Rayleigh mode is twofold degenerate at \bar{M} . The arrows indicate the sagittal plane part of the displacement pattern of the Rayleigh mode at \bar{M} for a wave vector along the $\langle 110 \rangle$ direction, which is indicated by the dashed diagonal line in (a). The shear horizontal part of the displacements is obtained by rotating the unit cell by an angle of 90° around an axis perpendicular to the surface. (c) The surface Brillouin zone. The high symmetry points and the directions are indicated in the irreducible part of the Brillouin zone.

normal can be changed by rotating the crystal. The incident beam is collimated to 0.28° and the scattered beam is collimated to 0.17° with respect to the crystal.

The base pressure in the target chamber was about 5×10^{-11} mbar. With the helium beam on the helium partial pressure increases to 3×10^{-8} mbar. Temperature measurements of the crystal were performed with a thin 0.1-mm diam. NiCr-Ni thermocouple. The thermocouple was attached to the crystal by inserting into a drilled hole which was plugged up tightly with KMnF_3 powder (see Fig. 2). A temperature stability of better than 50 mK was achieved by a computer controlled feedback system. The thermocouple was calibrated against liquid nitrogen and room temperature.

For time-of-flight (TOF) measurements a chopper can be moved into the incident beam between nozzle and crystal. Most of the measurements were performed at a beam energy of $E_i = 19.1$ meV (incident wave vector $k_i = 6.05 \text{ \AA}^{-1}$) and some at $E_i = 33.9$ meV ($k_i = 8.05 \text{ \AA}^{-1}$). The effective energy and wave-vector resolution depend on the incident angle and the energy loss.²³ The energy resolution is somewhat better than in the earlier work²² mainly due to the use of a shorter ionization region in the mass spectrometer. At an average value of $E_i = 19.1$ meV and incident angles near the specular direction the resolution was determined to be $\delta\Delta E = 0.5$ meV and $\delta\Delta K = 0.07 \text{ \AA}^{-1}$ (FWHM) for the longest axis of the resolution ellipsoid. Because of the large anisotropy of the resolution ellipsoid, however, points in the $(\Delta E, \Delta K)$ plane with $\delta\Delta E \approx 0.2$ meV and $\delta\Delta K \approx 0.01 \text{ \AA}^{-1}$ can be resolved under favorable kinematic conditions.²⁴

KMnF_3 was chosen for this initial study since it is one of the few perovskites which do not contain oxygen. Oxygen-containing perovskites like SrTiO_3 have the tendency to lose some of their oxygen on heating²⁵ and moreover the $\text{SrTiO}_3(001)$ surface seems to be chemical reactive.²⁶ The KMnF_3 crystals were obtained from Cavendish Laboratories, Oxford, U.K.²⁷

The crystals were cleaved under ultrahigh vacuum conditions *in situ* after bakeout of the chamber with the aid of an externally controlled forceps arrangement and for reasons discussed later, were never heated above 340 K after cleavage. Under these conditions the crystal surface was found to be entirely inert against contamination from the residual gas in the chamber. Previous experiments with crystals cleaved in air gave no satisfactory results since the crystal surface appeared to roughen or decompose during the subsequent bakeout of the chamber. Altogether we have used three crystals cut from the same boule.

Although our apparatus was equipped with a LEED and an Auger system neither of these standard surface techniques were employed to characterize the crystal surface. Because KMnF_3 is a good insulator a small amount of charge carriers must be generated to avoid charging of the surface. In previous work on SrTiO_3 this was done by a partial reduction of the crystal in a hydrogen atmosphere at elevated temperatures to form color centers²⁵ or by bombardment with electrons of several 100 V. The irradiation of the surface with an electron beam of the Auger or LEED system however introduces additional defects on the surface. As has been shown extensively in previous work the HAS specular intensity is very sensitive to the defect concentrations on the surface²⁸ and such defects would significantly attenuate the beam. For this reason only the entirely nondestructive helium beam was used to characterize the surface. The great sensitivity of HAS can be explained by the fact that a single surface defect has a large cross section which is much larger than the area of a substrate surface cell. The observation of no significant decrease of the specular and the Bragg peak intensities over periods of several weeks of measuring time indicates that the surface is very inert toward the residual gas.

HAS angular distributions provide a more direct method to detect small concentrations of inherent surface

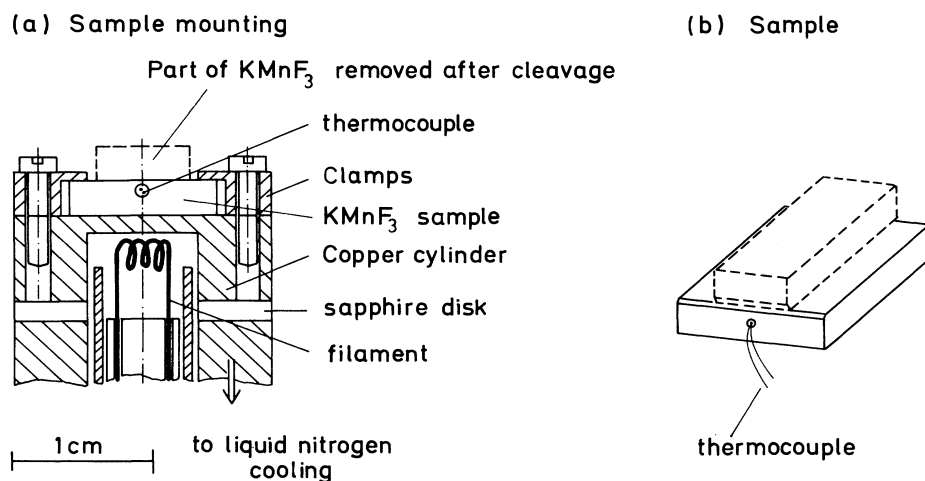


FIG. 2. (a) Schematic view of the sample holder. The copper cylinder can be cooled from behind. The dashed part of the crystal was removed when cleaving the crystal. The shape of the crystal prior to cleavage is drawn in (b).

defects which were always found to be present even on the surfaces of crystals cleaved in vacuum.^{21,29} Figure 3 shows a series of angular distributions across the specular peak and the first-order diffraction peak taken on successive days after cleaving the crystal. All measurements were done at a crystal surface temperature $T^s=320$ K and incident wave vector $k_i=6.05 \text{ \AA}^{-1}$ in the $\langle 110 \rangle$ azimuth direction. For the first 2 days the crystal was held at 320 K. Immediately after cleaving the crystal the specular peak and, less clearly, the diffraction peak showed broad satellite peaks. These satellites shifted with time toward the specular and the diffraction peak, respectively. After 2 days at 320 K these satellites had almost disappeared and the specular intensity increased. This process can be accelerated by heating the crystal up to 340 K for several hours. A possible explanation for the occurrence of these satellite peaks is the existence of small islands of the two different surface types—KF and MnF_2 —produced by the cleaving procedure (see Fig. 1). These islands may either grow with time or the smaller islands evaporate resulting in a smaller number of larger islands. The decrease of the broad intensity maximum seen at $\theta_i \approx 52^\circ$ is discussed in Sec. III. A sensitive way to

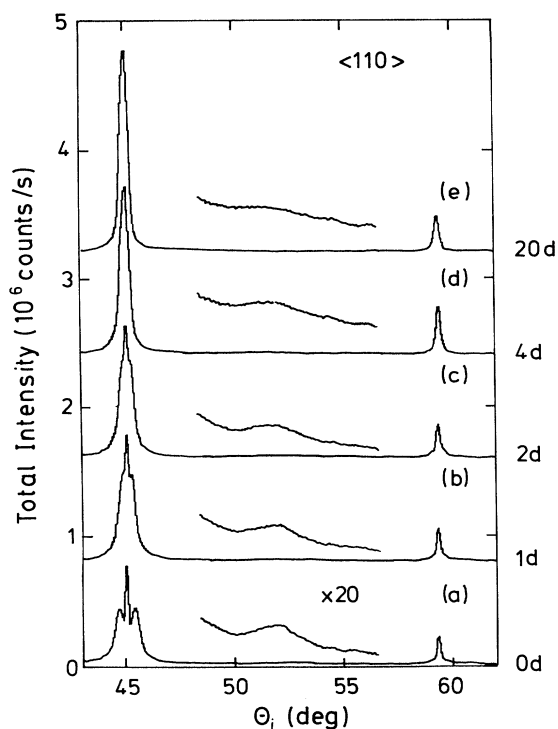


FIG. 3. He atom angular distributions of the total intensity along the $\langle 110 \rangle$ direction at different times after cleavage: (a) immediately after cleavage, (b) after 1 day, (c) after 2 days, (d) after 4 days, (e) after 20 days. All angular scans were measured at 320 K and with an incident beam wave vector of $k_i=6.05 \text{ \AA}^{-1}$. While the intensity of the specular and the Bragg peaks at $\theta_i=59.4^\circ$ increases, the intensity around the superstructure peak position at $\theta_i=52.2^\circ$ of the low temperature phase decreases.

detect the height and density of surface steps is provided by the measurements of the specular intensity as a function of the beam energy. Constructive and destructive interference of waves scattered from terraces separated by steps of different heights can interfere and lead to an oscillatory behavior.³⁰ Thus the amplitude of the specular intensity oscillations is a measure of the step concentration and the spacing a measure of the step height. The specular intensity versus the incident wave vector of the He beam plotted in Fig. 4 reveals large oscillations due to interferences between islands of different height. Although the lattice spacing of the two levels is the same the analysis of these oscillations gives, in fact, two different step heights of 2.36 and 1.83 \AA which add up to the lattice constant $a=4.19 \text{ \AA}$ (Ref. 31) of the cubic unit cell, i.e., the distance between two KF or MnF_2 faces. Thus, because of the symmetry of the unit cell (see Fig. 1) a single step corresponds to a distance between atomic planes of $\frac{1}{2}a=2.095 \text{ \AA}$. The observed difference in step heights cannot be explained by the small difference in the relaxation of the positions of the nuclei of about 1% of the lattice constant or less.¹⁷ To understand the difference we note that the He atoms are scattered from the small charge distributions of the surface atoms of the order of 10^{-4} electrons/a.u.³ which prevail at distances of 3–4 \AA from the nuclei of the outermost layer.³² Thus the observed step height difference of 0.26 \AA must most

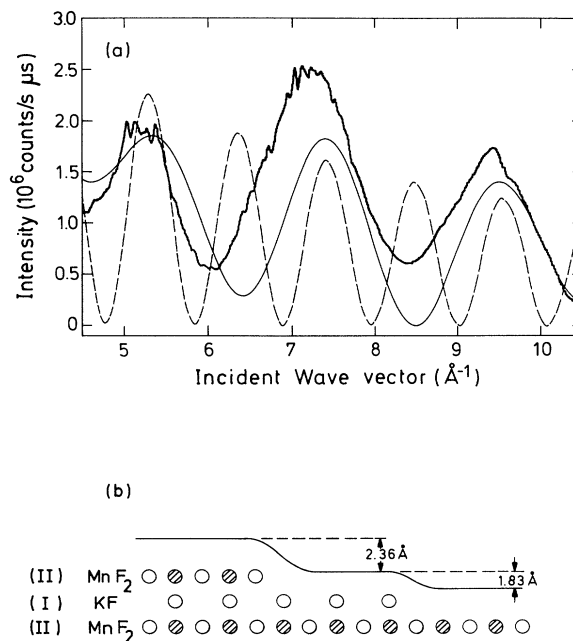


FIG. 4. (a) He atom specular intensity versus incident wave vector at 310 K. The large oscillations are due to interference between adjacent terraces. The smooth solid curve represents the results of a simulation with two different steps of heights of 1.83 and 2.36 \AA^{-1} with equal concentration. For comparison the dashed curve shows a simulation based on a single step height equal to the unit cell of 4.19 \AA^{-1} . (b) illustrates the proposed origin of the two different step heights.

likely be attributed to differences in the spill out of the charge distributions for the two surfaces which lead to different effective average turning points of the He atoms with respect to the position of the nuclei. The observed difference in the step heights between KF on top of MnF_2 (1.83 Å) and vice versa (2.36 Å) is most likely due to the different number of F^- ions, which dominates the interaction with the He atoms³³ in the KF and MnF_2 layers. The good fit of spacing of the undulation in the specular intensity shown by the smooth solid curve in Fig. 4 also rules out the existence of double steps and we estimate that they contribute less than 10% of the single steps. A greater amount would lead to additional closer lying maxima in the intensity versus incident wave-vector curve. Moreover the data are only consistent with the assumption that both types of surfaces contribute with approximately equal weight to the scattering. Since the measurements were done immediately after cleavage and positional adjustment of the crystal there is no reason to assume an inequality in the areas of the two surface types. Repeating the measurement after several days gave basically the same result. This changes only when heating the crystal above room temperature as is discussed in Sec. V.

In principle it is possible to deduce the terrace width distribution and the step concentration from the shape and amplitude of the broad satellite peaks close to the specular peak and the Bragg peaks in the angular distributions and the variation of the specular intensity with the incident wave vector in a similar way as in the spot profile analysis of LEED measurements.³⁴ We did not attempt such an analysis because of the relatively fast change of these structures with time. Moreover the initial concentrations were different for the different crystal surfaces used in this investigation. In the present case the analysis of the data is greatly complicated by the occurrence of the two different step heights on the surface. From the wave-vector position of the satellite peaks in Fig. 3 an initial average width of the terraces of the order of ≈ 100 Å can be roughly estimated.

III. CRITICAL SCATTERING AND TEMPERATURE DEPENDENCE OF THE SUPERSTRUCTURE PEAKS

A. Determination of the surface transition temperature

Figure 5 shows a series of angular distributions direction of the total scattered intensity in the $\langle 110 \rangle$ direction at different temperatures. Some weak extra structures are visible between the Bragg peaks even at 240 K. Most of these are inelastic maxima due to "kinematic focusing" which results from special kinematic conditions.³⁵ With decreasing temperatures additional Bragg peaks grow at the half-order positions below 180 K, increasing in intensity on further cooling. The inelastic background and especially the structures due to the kinematic focusing effects makes it difficult to determine the exact surface phase transition temperature from the total scattering intensity. Therefore, the inelastic part of the total scattered intensity was separated off by the time-of-flight tech-

nique. Figure 6 shows the intensity in the range of ± 10 μs around the flight time corresponding to the elastic scattered peak which has been plotted versus the incident angle around the $(\frac{1}{2}\frac{1}{2}0)$ superstructure peak. This time interval is equivalent to an energy range of ± 0.25 meV which is about equal to the half width of the instrumental energy resolution. Figure 6 shows that a broad peak increases gradually with decreasing temperature. At the highest temperature of $T=310$ K this broad very weak maximum is still observable at a parallel momentum transfer of $\Delta K=1.06$ Å⁻¹. With decreasing temperature the width of this peak decreases slightly. This is hard to see in Fig. 6 because of the very low intensities. At 190 K and below an additional sharp Bragg peak grows on top of the broad one. The width of this additional superstructure peak is determined by the angular resolution of the apparatus and the intensity of this peak increases very rapidly on further cooling. The intensity of the superstructure peak increases nearly continuously from the phase transition at 191 ± 1 K (see below) as the temperature is reduced further.

To determine the order of the phase transition, the

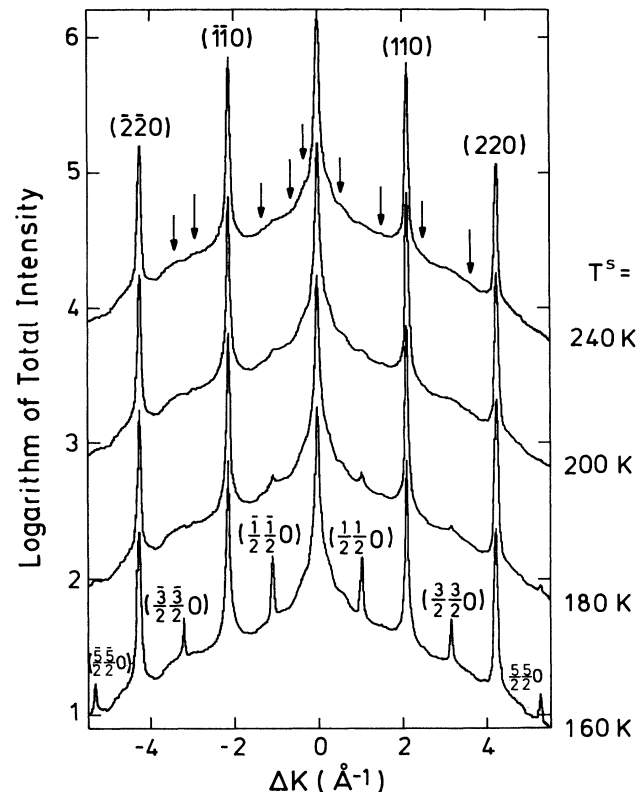


FIG. 5. Series of total intensity angular distributions along the $\langle 110 \rangle$ direction converted to a wave vector (ΔK) scale at various crystal temperatures. Below 180 K the half-order superstructure peaks are clearly visible. The weak additional structure between the diffraction peaks indicated by arrows in the $T^s=280$ K angular distribution, is due to "kinematic focusing" effects. For all angular distributions the incident wave vector is $k_i=6.05$ Å⁻¹. Note the logarithmic intensity scale.

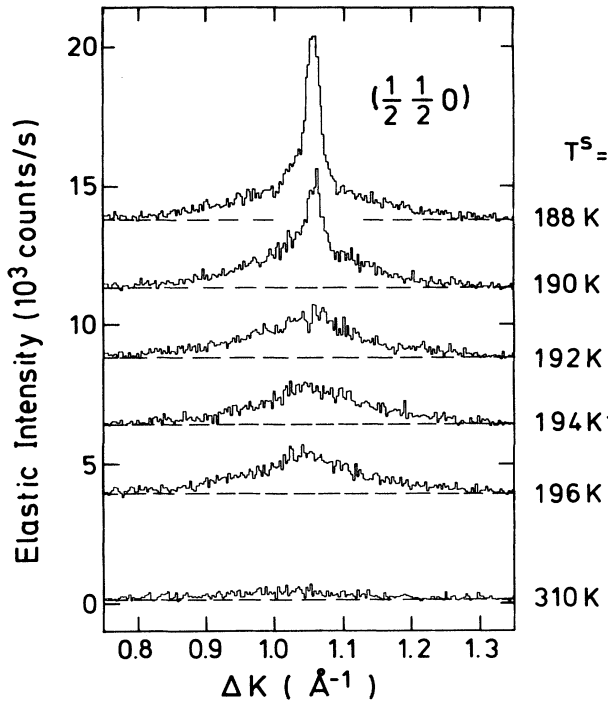


FIG. 6. Series of elastic angular distributions in the vicinity of the $(\frac{1}{2}\frac{1}{2}0)$ diffraction peak position at different crystal temperature. $k_i=6.05 \text{ \AA}^{-1}$. The energy width of the elastic window is $\pm 0.25 \text{ meV}$. The dashed line indicates the constant background at 310 K.

elastic intensity of the (110) Bragg peak was also measured as a function of temperature. The result is shown in Fig. 7 together with the intensity of the peak at the $(\frac{1}{2}\frac{1}{2}0)$ position. At the phase transition temperature a finite jump is clearly seen in the intensity of the (110) Bragg peak indicating a first-order transition. For the $(\frac{1}{2}\frac{1}{2}0)$ superstructure peak we cannot rule out a possible small discontinuous jump at T_c^s which is not resolved. On further cooling this peak appears to grow nearly linear in intensity. Therefore we conclude that the surface phase transition is of weak first order as in the bulk.³ The extrapolated linear rise of the $(\frac{1}{2}\frac{1}{2}0)$ peak back to zero intensity indicates the surface phase transition temperature to be $T_c^s=191\pm 1 \text{ K}$. This transition temperature remains unchanged within the experimental accuracy even after several cooling and heating cycles through the phase transition. This value lies $3.5\pm 1 \text{ K}$ above the highest published value for the bulk phase transition of $T_c^b=187.5\pm 0.08 \text{ K}$.⁴ Since the difference is greater than the reported variations of the bulk transition temperature and greater than the estimated errors in our temperature measurements, we feel that this difference is significant. However, it is known from bulk measurements, that certain types of defects can significantly change the transition temperature.³⁶ Since as discussed in connection with Figs. 3 and 4 the defect concentration of the cleaved $\text{KMnF}_3(001)$ surface is rather high, we can therefore not entirely rule out that the increased transition temperature at the surface is due to a larger concentration of defects

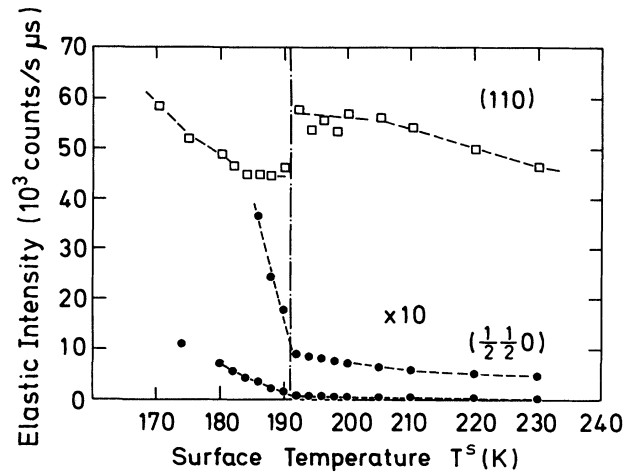


FIG. 7. Elastic intensity of the (110) Bragg peak and the $(\frac{1}{2}\frac{1}{2}0)$ superstructure peak as a function of the crystal temperature. $k_i=6.05 \text{ \AA}^{-1}$. The $(\frac{1}{2}\frac{1}{2}0)$ data are also plotted in a magnified scale.

at the surface. For this reason a direct comparison of the T_c^s and T_c^b values on the same crystal would be highly desirable but was not possible in the present experiments.

B. Theoretical aspects of phase transitions at surfaces

The critical behavior of the order parameter η , the susceptibility χ , and other properties in the bulk can be described by power laws with certain critical exponents which depend only on the symmetry of the system. Thus, the relevant quantities of all second-order phase transitions in the same universality class can be described by power laws

$$\eta = \eta_0 \left[\frac{T - T_c}{T_c} \right]^\beta, \quad \chi = \chi_0 \left[\frac{T - T_c}{T_c} \right]^\gamma, \quad (1)$$

with universal exponent β and γ . The surface breaks the translational symmetry of the crystal perpendicular to the surface plane. As a consequence the local quantities such as the displacement from lattice sites may differ at the surface from the values deep in the bulk. Surface probes such as LEED and HAS measure the order parameter and the susceptibility at the surface denoted as η_1 and $\chi_{1,1}$ in Ref. 37 describing the critical behavior at the surface. The critical behavior of η_1 and $\chi_{1,1}$ differ from that of the surface order parameter η_s and surface susceptibility χ_s , which describe the integral difference between the local quantities and the quantities deep in the bulk.

At the surface the interaction between the atoms is changed because of missing neighbors compared to the bulk. Therefore the free energy per unit cell is reduced at the surface. However, relaxation of the atomic layers can more than compensate for the reduction and lead to an increase in the free energy. In mean-field theory this

change can be accounted for by the so-called extrapolation length λ .³⁷ Depending on whether λ is positive, infinite, or negative, different critical behavior are expected to occur at the surface. In the case of an ordinary phase transition $\lambda > 0$ and the magnitude of the order parameter is reduced with respect to its value in the bulk. In the case of the special phase transition $\lambda = \infty$ and the order parameter is unchanged at the surface, whereas in the extraordinary phase transition $\lambda < 0$ the order parameter is enlarged in a thin layer at the surface and decays to a constant nonzero value in the bulk. In this latter situation already at a temperature T_c^s above the bulk transition temperature T_c^b a transition occur in a thin layer of the surface preceding the extraordinary transition. This transition is called a surface phase transition. In the temperature interval between T_c^s and T_c^b the order parameter is only nonzero at the surface and decays exponentially with an exponent proportional to λ into the bulk where the transition has not yet occurred.

These phase transitions have different critical exponents. Mean-field theory yields the following exponents for the local order parameter η_1 and for the local susceptibility $\chi_{1,1}$: $\beta_1=1$, $\gamma_{1,1}=-\frac{1}{2}$ for the ordinary transition; $\beta_1=\frac{1}{2}$, $\gamma_{1,1}=\frac{1}{2}$ for the special transition; $\beta_1=1$, $\gamma_{1,1}=0$ for the extraordinary transition and $\beta_1=\frac{1}{2}$, $\gamma_{1,1}=\frac{1}{2}$ for the surface transition.³⁷ The values for the bulk transition in the mean-field approximation are $\beta_b=\frac{1}{2}$ and $\gamma_b=1$.³⁸

In bulk KMnF_3 the order parameter is three dimensional and the Heisenberg model is approximately applicable.³⁹ The theoretical exponents for this model are $\beta_b=0.365$ and $\gamma_b=1.386$,⁴⁰ i.e., the β_b is smaller and γ_b is greater than the mean-field value. The exact critical exponents β_1 and $\gamma_{1,1}$ for the Heisenberg model with surface anisotropy are not known. However, Monte Carlo calculations reveals values about $\beta_1=0.8\pm 0.1$ for the ordinary transition.⁴¹ Renormalization-group results are more accurate and give $\beta_1=0.85\pm 0.03$ and $\gamma_{1,1}=-0.28\pm 0.03$.⁴² In comparison the values for the 3D Ising model are $\beta_1=0.79\pm 0.1$ and $\gamma_{1,1}=-0.33\pm 0.1$. For the Heisenberg model there exists no long-range order above T_c^b and therefore no surface transition. However, an anisotropy term in the Hamiltonian may restore surface order above T_c^b .³⁷

C. Superstructure peak intensities below the phase transition temperature T_c^s

In scattering experiments with point scatterers like x-rays and neutrons the interaction potential can be simply described as a sum of a pairwise interaction potentials between the projectile and a sample atom and the scattered intensities can be calculated within the Born approximation. Therefore, the critical exponent β can be derived directly from the temperature dependence of the measured intensity of the superstructure peaks induced by the transition. In the case of HAS neither the assumption of an interaction potential as a sum of atomic pair potentials nor the Born approximation holds in general because the He atoms are scattered from the extended

charge distribution of the surface atoms. However, it has been shown experimentally that the pair potential ansatz is nevertheless a remarkably good approximation for ionic crystal surfaces.³³ For helium scattering the Born approximation must be replaced by the distorted wave Born approximation (DWBA) where the z component of the scattered plane wave is replaced by the true wave function of the lateral averaged interaction potential.⁴³ It can be shown, that in the DWBA the scattered intensity at the superstructure peak is still proportional to the square of the order parameter as will be demonstrated in the Appendix. The above considerations indicate that in general the cross section does not separate into a temperature independent scattering matrix element and a Debye-Waller factor containing all the temperature dependence except that of the order parameter. For every special case one has to check experimentally the validity of the extrapolation of the temperature dependence from high temperatures to the region around the transition temperature. Because of such inherent approximations the results on critical exponents obtained with HAS do not necessarily have the same accuracy, as for example, those obtained from neutron or x-ray scattering experiments. Figure 8 shows that the intensities of the main Bragg peaks have no strong temperature dependence aside from the small dip close to the transition between 130 and 210 K. This fortuitous result enables us to ignore completely the influence of the Debye-Waller factor near the transition temperature.

Below the phase transition temperature the intensity of the superstructure peaks increases by about 1.5 orders of magnitude as the temperature drops from the transition down to ≈ 140 K which can be seen in Fig. 7. For pur-

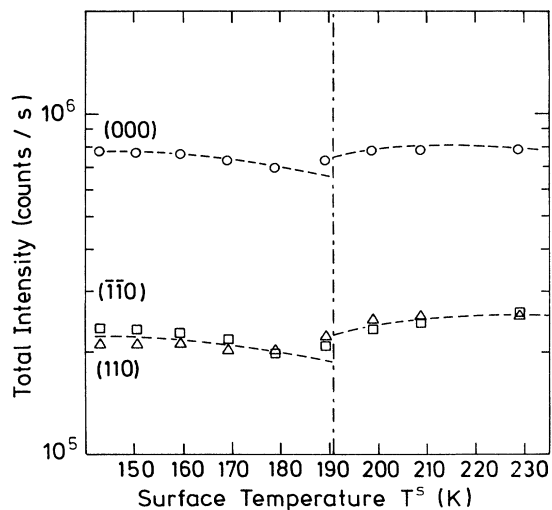


FIG. 8. Semilogarithmic plot of the total intensities of the specular (circles) and two main Bragg peaks [(1-10) squares and (110) triangles] as a function of crystal temperature. The vertical dot-dashed line indicates the experimental determined temperature of the phase transition.

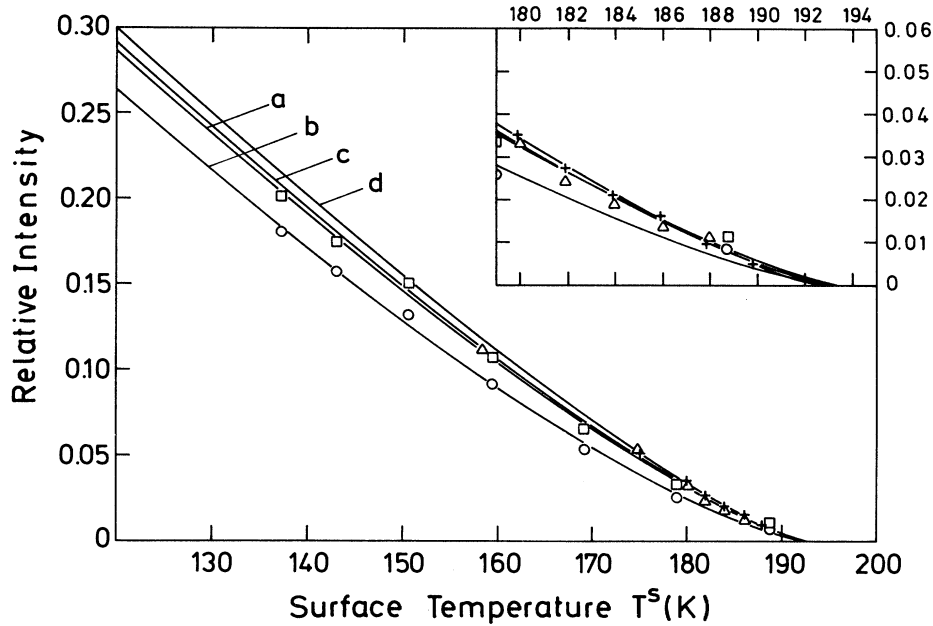


FIG. 9. Normalized intensities of the superstructure peaks vs crystal temperature. The solid lines are fits to a power law. Curves *a* and *b* were obtained from fits of peaks in the angular distributions of the total intensity with $k_i = 8.05 \text{ \AA}^{-1}$ for the $(\frac{1}{2}\frac{1}{2}0)$ (squares) and $(\frac{1}{2}\frac{1}{2}0)$ (circles) superstructure peaks. Curve *c* (triangles) and *d* (crosses) were obtained from elastic angular distributions with $k_i = 6.05 \text{ \AA}^{-1}$ at the $(\frac{1}{2}\frac{1}{2}0)$ superstructure peak where the inelastic part of the intensity was separated off by the time-of-flight technique with an energy window of $\pm 0.25 \text{ meV}$. The curves and data points are normalized to 1 at 0 K. The region around T_c is plotted in the inset in a magnified scale. As discussed in the text the critical exponent β_1 is the same for all four curves.

poses of determining the critical exponent β_1 in Fig. 9 the normalized intensities of the $\{\frac{1}{2}\frac{1}{2}0\}$ superstructure peaks are plotted versus the temperature. In each of the four sets of data points the intensities of the superstructure peaks has been integrated over the peak width and divided by the factor I_0 of the fit, so that the intensity extrapolated to 0 K is 1. This was done to compare data obtained by the different methods explained below. The data corresponding to curves *a* [for the $(\frac{1}{2}\frac{1}{2}0)$ peak] and *b* [for the $(\frac{1}{2}\frac{1}{2}0)$ peak] are obtained from angular distributions of the total intensity. Close to the transition it is hard to get reliable values for the superstructure peaks due to the relatively large background. In order to circumvent this problem, the time-of-flight technique was used to separate off the inelastic part. These data for the elastic peaks are labeled as curves *c* and *d* [both for the $(\frac{1}{2}\frac{1}{2}0)$ peak]. Whereas prior to the measurements of curves *a*, *b*, and *c* the crystal was never heated higher than 320 K after cleaving, the data of curve *d* were obtained after annealing the crystal at 340 K for several hours which smoothens the crystal surface as reported above. In all cases the contributions from the inelastic and diffuse background have been interpolated and subtracted off. The solid lines are least-square fits of the data points to a power law:

$$I = I_0 \left(\frac{T - T'_c}{T'_c} \right)^{2\beta_1} \quad (2)$$

with the fit parameters I_0 , T'_c , and β_1 . We note that the absolute intensities of the experimental data points corresponding to curve *d* are increased approximately by a factor of 2 with respect to curve *c* but that β_1 remains unchanged. Obviously the different defect concentration has no influence to the critical behavior. The derived results for β_1 for all four curves are presented in Table I. In the evaluation of the intensities we have neglected completely the influence of the Debye-Waller factor. For curves *a* and *b* an additional value of β_1 is listed. This value was obtained by accounting approximately for the Debye-Waller factor by dividing the superstructure peak intensity by the specular intensity. Within the experimental errors there are no significant differences in the

TABLE I. Summary of the measured values of the extrapolated temperature T'_c and the critical exponent β_1 .

Curve	Bragg peak	T'_c	β_1
<i>a</i>	$(\frac{1}{2}\frac{1}{2}0)$	193.6 ± 1.5	0.65 ± 0.08
	with Debye-Waller correction	194.3 ± 1.5	0.62 ± 0.08
<i>b</i>	$(\frac{1}{2}\frac{1}{2}0)$	193.3 ± 1.8	0.68 ± 0.10
	with Debye-Waller correction	193.2 ± 1.5	0.64 ± 0.08
<i>c</i>	$(\frac{1}{2}\frac{1}{2}0)$	193.1 ± 0.3	0.64 ± 0.03
<i>d</i>	$(\frac{1}{2}\frac{1}{2}0)$	192.5 ± 0.3	0.62 ± 0.02
Averages:		192.8 ± 0.3	0.63 ± 0.03

value of β_1 and T'_c with respect to the uncorrected values of curves *a* and *b*. The fitted transition temperature T'_c is about 2 K higher than the true measured surface transition temperature. This difference is due to the weak first-order character of the transition.

Our average value for the surface $\beta_1 = 0.63 \pm 0.03$ is lower than the mean-field value expected for an extraordinary phase transition ($\beta_1 = 1$) but more than two times larger than the experimental bulk value of $\beta_b = 0.26 \pm 0.02$ (Ref. 4) and $\beta_b = 0.2857 \pm 0.0006$.⁴⁴ The theoretical bulk value is $\beta_b = 0.365$ in the Heisenberg model.⁴⁰ Because T'_c is very close to T_c^b it is conceivable that there are contributions from the two phase transitions, the surface and the extraordinary transition. If this is the case then the observed value is an average value of the two β_1 's of both transitions.

We note that for the Heisenberg model there exists no surface transition. However, the large experimental value of β_1 is also consistent with an ordinary phase transition. The theoretical predicted value for this case, $\beta_1 = 0.85 \pm 0.03$,⁴² is higher than the experimental value but this discrepancy is also present in the bulk and is explained by fact that the bulk transition is of slightly first order and occurs in the vicinity of a tricritical point at which the critical exponents are changed.⁴⁴ This is also true for the surface. Scaling the theoretical value for β_1 with the quotient of the theoretical and experimental value for β_b gives an estimated value of $\beta_1 \approx 0.67$, which is in reasonable agreement with our experimental result. All this is valid only for the case of an ordinary phase transition. But if the difference of about 3.5 K in the transition temperature T_c^s with respect to the bulk transition temperature T_c^b is real an extraordinary phase transition occurs preceded by a surface transition at a higher temperature. There exists no theoretical predictions except those of the mean-field theory for the critical exponents for this case and because of the small difference between T_c^s and T_c^b it might be difficult to get meaningful quantitative results on β_1 .

D. Critical scattering above T_c^s

Above T_c^s the elastic intensity at the superstructure peak position does not vanish entirely and the remaining small broad signal has a strong temperature dependence as can be seen in Figs. 6 and 7. A part of this intensity is due to the diffuse scattering from defects such as impurities, vacancies, and steps. The temperature dependence of this contribution is however not expected to have a singularity at T_c^s and can be well described by an exponential Debye-Waller factor. Since it has no strong angular dependence it only contributes to the uniform background indicated as dashed lines in Fig. 6. The remaining structural part is attributed to the critical scattering. As discussed in the Introduction in the bulk the central component ("central peak") at temperatures close to T_c^b has a very small width both in energy and wave vector which is even smaller than the resolution of ordinary neutron experiments of typically 0.1 meV and 0.015 \AA^{-1} .¹⁴ Since our resolution both in energy and wave vector is

less this central component could not be separated off from the ordinary soft phonon induced critical scattering. Thus, the intensity of the observed broad peak is probably a mixture of the central peak and the overdamped soft surface phonon, as will be discussed in Sec. IV.

Due to the kinematic conditions in our experiment no soft phonon induced broadening of the diffuse elastic peak could be observed at the superstructure peak position. Figure 10 shows TOF spectra of the elastic peak at the \bar{M} point at increasing temperatures from $T^s = 310 \text{ K}$ for the lowest curve to $T^s = 188 \text{ K}$ for the topmost curve. No broadening of this peak due to contributions of the soft mode are observable along this scan curve. As has been shown by Gesi *et al.*⁴⁵ the width of the diffuse scattering around a half-order peak is very anisotropic and is much larger in the $\bar{M}\bar{X}$ direction. The half width of the out-of-plane wave-vector resolution is with $\delta\Delta K_{\perp} = 0.06 \text{ \AA}^{-1}$ not larger than the in-plane resolution. Therefore the broad tail in the $\bar{M}\bar{X}$ directions is not included in the TOF spectra.

In Fig. 11 the intensity and the wave vector half width of this peak are plotted in a double logarithmic scale versus the reduced temperature $(T - T_c^s)/T_c^s$. The uni-

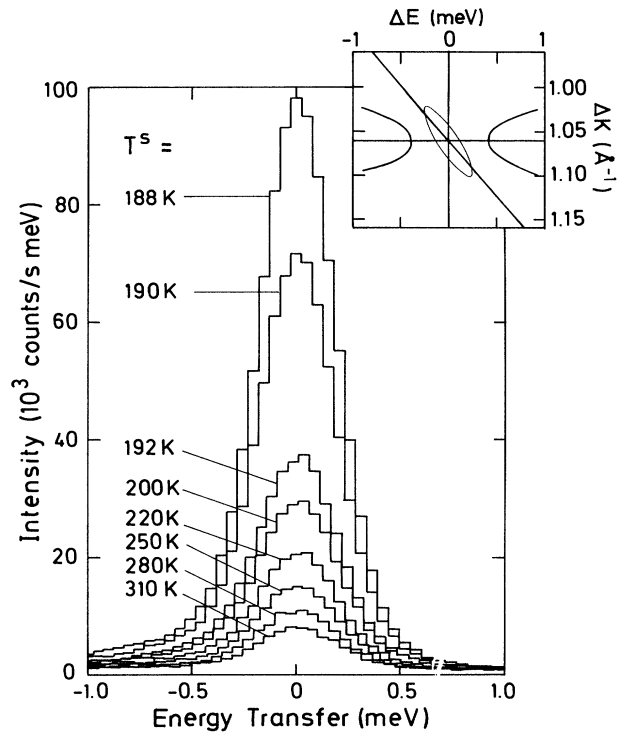


FIG. 10. A series of TOF spectra around the $(\frac{1}{2}\frac{1}{2}0)$ ($\theta_i = 37.95^\circ$) superstructure peak at various crystal temperatures measured with $k_i = 6.05 \text{ \AA}^{-1}$. While the intensity increases with decreasing surface temperatures no broadening of the peak is observable. The scan curve and the half width of the resolution function for these TOF spectra are depicted in the inset together with a schematic plot of the soft phonon dispersion curve. The elliptic curve represents the half width of the resolution function.

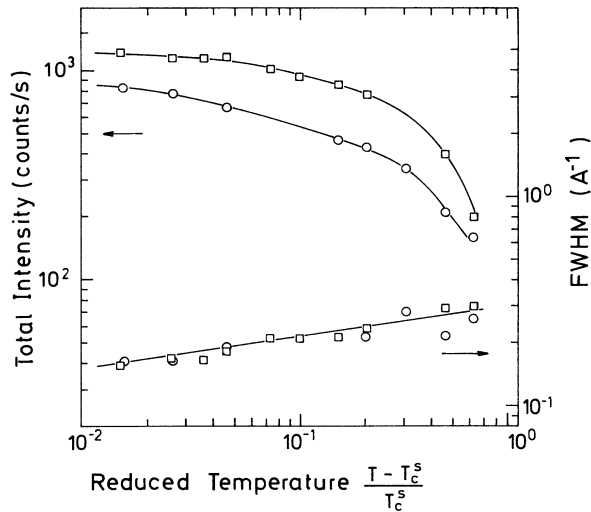


FIG. 11. Elastic intensity (the two upper curves, left scale) and full width at half maximum FWHM (the lower curve, right scale) of the critical scattering at the $(\frac{1}{2}\frac{1}{2}0)$ (squares) and $(\frac{1}{2}\frac{1}{2}0)$ (circles) superstructure peak as a function of the reduced temperature $(T - T_c^s)/T_c^s$ with $T_c^s = 191$ K. The solid lines are guidelines to the eye. The difference in the intensities of the critical scattering of the two curves are due to different defect concentrations of the sample. The measurements of the $(\frac{1}{2}\frac{1}{2}0)$ peak were done at a later time.

form background indicated as a dashed line in Fig. 6 has been subtracted off. The peaks were fitted by a Gaussian curve. The intensity of the critical scattering for the $(\frac{1}{2}\frac{1}{2}0)$ is lower than the intensity for the $(\frac{1}{2}\frac{1}{2}0)$ superstructure peak because the data for the $(\frac{1}{2}\frac{1}{2}0)$ peak were taken at a later time after cleavage of the crystal. As mentioned in Sec. II the intensity of the critical scattering decreases while the intensity of the Bragg peaks increases at the expense of the broad satellites close to these peaks which are due to defects. This observation and the lack of broadening of the diffuse elastic peak in the TOF spectra suggests that a major part of the critical scattering was induced by defects which is further confirmed by the fact that the soft phonon induced part has only a small cross section in helium scattering as will be discussed in Sec. IV. Because of these reasons no attempt was made to derive values for $\gamma_{1,1}$.

IV. DISPERSION CURVES AND TEMPERATURE DEPENDENCE OF THE RAYLEIGH PHONON

A. Phonon dispersion curves in the high temperature phase

In this section we discuss the surface phonon dispersion curves resulting from TOF measurements in the $\langle 100 \rangle$ and $\langle 110 \rangle$ directions. While in the $\langle 100 \rangle$ direction no strong temperature dependence is expected, in the $\langle 110 \rangle$ direction the surface Brillouin zone is reduced by one half in the low temperature phase consistent with the observed superstructure peaks. Since the phase transition in the bulk is more of the displacive character, we expect-

ed that analogous to the bulk behavior a softening of a particular phonon mode should also be observable at the surface. Before we discuss the temperature dependence of the phonon modes in the $\langle 110 \rangle$ direction we first report the experimental results on the high temperature phase.

Figure 12 shows a series of TOF spectra along the $\langle 100 \rangle$ direction at 320 K. The phonon peaks can be identified with the aid of the scan curves shown at the top of Fig. 12. These indicate for each incident angle θ_i the kinematically allowed points in the energy transfer-parallel momentum transfer plane. Also shown as solid lines at the top of Fig. 12 are the approximate dispersion curves which can be derived from the scattering angles and the position of the phonon peaks. Aside from a strong Rayleigh mode with a maximum frequency of 9.5

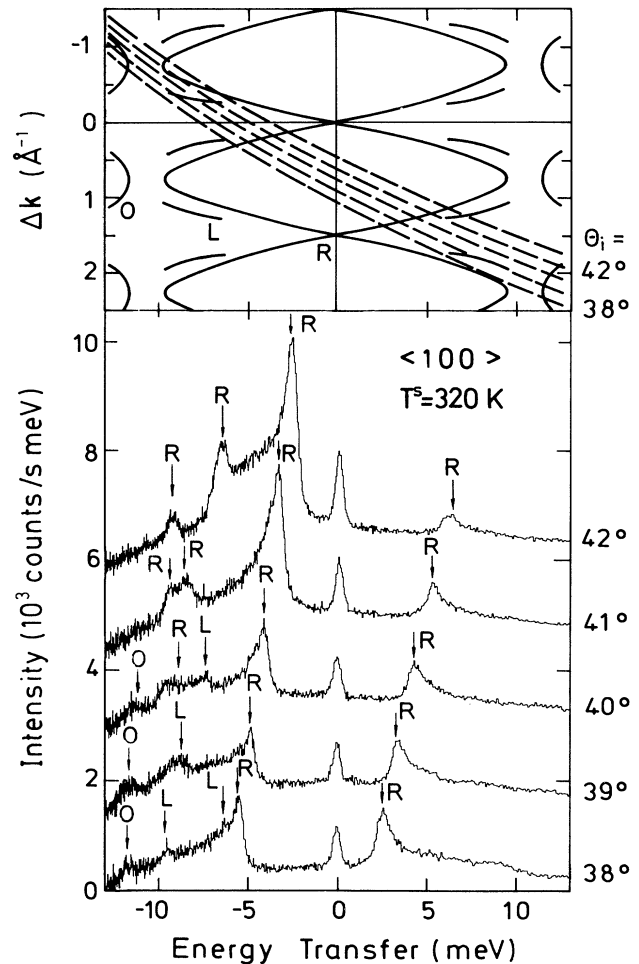


FIG. 12. A series of TOF spectra taken at $\Delta\theta_i = 1^\circ$ intervals converted to an energy transfer scale in the $\langle 100 \rangle$ direction at $T^s = 320$ K ($k_i = 6.07 \text{ \AA}^{-1}$). For the assignment of the phonon peaks the scan curves are plotted together with the dispersion curves derived from the data. The phonon peaks of the different branches are labeled as R for the Rayleigh mode, L for the longitudinal resonance, and O for the optical in the TOF spectra.

meV two additional weak modes are observed. One lies about 2 meV above and parallel to the Rayleigh mode and is only seen at intermediate wave vectors Q . Energy loss peaks for this mode are clearly observed in the TOF spectra at $\theta_i = 40^\circ, 39^\circ$, and 38° at positions corresponding to negative ΔK values. In the $\theta_i = 38^\circ$ TOF spectrum a very weak peak indicated by an arrow close to the Rayleigh loss peak can be attributed to the $+\Delta K$ branch of the same mode. At lower temperatures this peak becomes more apparent (see Fig. 13 below). The highest mode is nearly flat at a frequency of about 12 meV. In addition an elastic peak is seen at $\Delta E = 0$ due to scattering from defects.²¹ Figure 13 shows the same series of TOF spectra as in Fig. 12 but at 140 K. No changes in peak position were observed when the crystal was cooled below the phase transition temperature. The strong increase of the diffuse elastic peak relative to the inelastic peaks may be explained by the fact that in the low temperature phase the defect concentration is enlarged due to the creation of domain walls at the phase transition. The increase of the one phonon intensities at the expense of the multiphonon background is attributed to the reduced Debye-Waller factor. Otherwise no significant changes are apparent.

Before discussing the dispersion curves we note that since the surface breaks the bulk symmetry the projected bulk bands do not have the same high symmetry as the corresponding bulk bands in directions parallel to the surface. In the two high symmetry directions of the (001) surface, the $\bar{\Gamma X}$ ($\langle 100 \rangle$) and the $\bar{\Gamma M}$ ($\langle 110 \rangle$) directions,

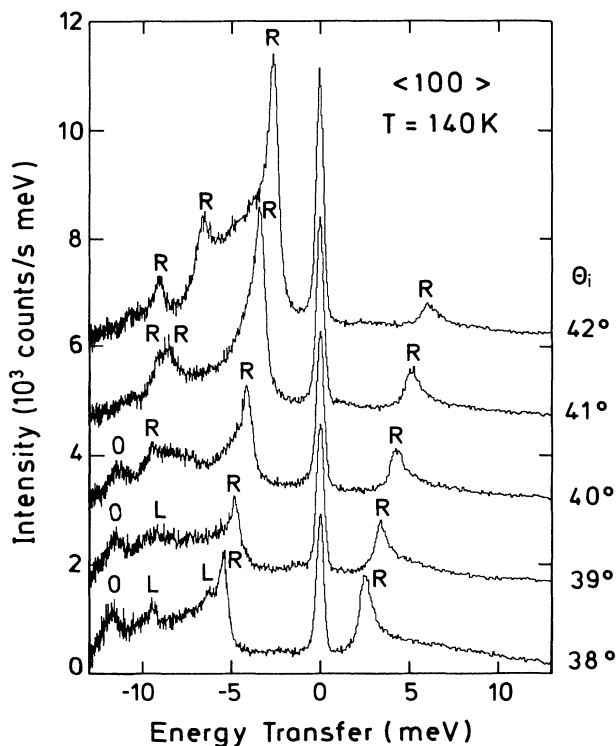


FIG. 13. Same as in Fig. 12 but at 140 K.

the symmetry group is C_s , i.e., the mirror plane in the sagittal plane is the only symmetry operation which leaves the wave vector invariant. Surface and bulk modes either transform into themselves, in which case they are called sagittal plane modes, or change sign in which case they are called shear-horizontal modes. It is only possible to distinguish between these two symmetries of the bulk bands and surface modes. Nevertheless we denote every projected bulk band by the symmetry of the bulk mode in the corresponding direction parallel to the surface keeping in mind that the symmetry does not hold strictly for the whole projected band. However, the surface mode which splits off from a particular bulk band has a similar displacement pattern as the bulk mode in that direction if it is not separated too much from the corresponding bulk mode. This enables us to approximately assign a polarization to most surface modes without any calculation.

In Fig. 14 all data points in the $\langle 100 \rangle$ directions are plotted in a plot of energy versus phonon wave vector together with the theoretical predicted surface modes.¹⁷ The dashed lines correspond to theoretical surface modes of surface I and the solid lines to theoretical modes of surface II. The Rayleigh mode for both surfaces are nearly identical. The bulk modes in the $\langle 100 \rangle$ direction⁴⁵ are indicated by hatched boundaries, which are the

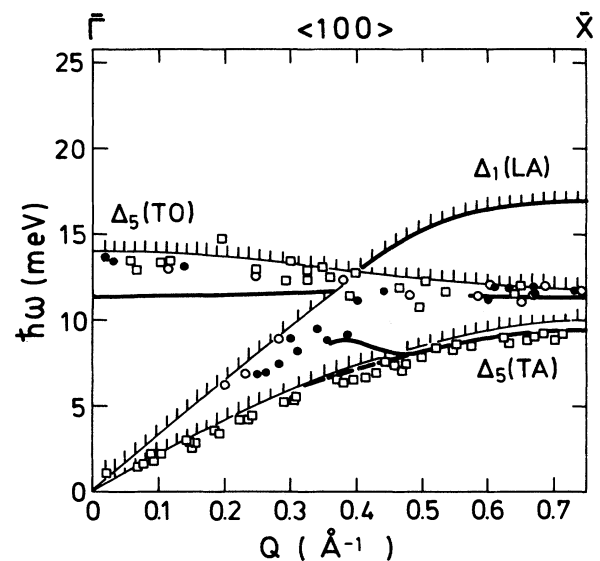


FIG. 14. Comparison of experimental and theoretical dispersion curves in a surface phonon energy $\hbar\omega$ vs wave vector Q plot in the $\langle 100 \rangle$ direction. The boundaries represent the edges of the bulk bands. The notation refers to the mode symmetries in the $\bar{\Gamma X}$ direction in the bulk. The heavy dashed and solid lines are the predicted dispersion curves of the surface modes (Ref. 17) for surface I and surface II, respectively. The squares correspond to measurements at $k_i = 8.05 \text{ \AA}^{-1}$ and $T^s = 165 \text{ K}$, the open circles to measurements at $k_i = 6.07 \text{ \AA}^{-1}$ and $T^s = 140 \text{ K}$ and the solid circles to measurements at $k_i = 6.07 \text{ \AA}^{-1}$ and $T^s = 320 \text{ K}$. For the Rayleigh mode only the data at $k_i = 8.05 \text{ \AA}^{-1}$ and $T^s = 165 \text{ K}$ are plotted since the other measurements were indistinguishable from these points.

edges of the projected bulk bands except for the $\Delta_5(\text{TA})$ mode at wave vectors above $\approx 0.5 \text{ \AA}^{-1}$. Because of the strong softening of the transverse acoustic Σ_3 (TO) mode in the $\langle 110 \rangle$ direction the projected bulk modes, not shown in Fig. 14, extend to lower energies than the $\Delta_5(\text{TA})$ mode in the same region of wave vectors. This band has shear-horizontal polarization and is not excited in the sagittal plane scattering for surface I. For surface II their excitation is not forbidden by symmetry but we did not observe any intensity corresponding to these modes. The Δ_5 mode is twofold degenerate in the $\langle 100 \rangle$ direction and represents the band edge of the sagittal plane polarized bulk band.

All the experimental data points in Fig. 14 lie very close to bulk band edges so that the experimentally observed surface modes are easily assigned to the corresponding bulk modes. Whereas the experimentally observed Rayleigh mode is slightly below the transverse acoustic Δ_5 bulk mode the flat mode is close to the Δ_5 bulk transverse optical mode and well above the predicted location of the corresponding surface mode. In the phonon wave-vector region between 0.25 and 0.4 \AA^{-1} a third mode can be resolved. This mode lies slightly below the longitudinal acoustic bulk band edge and thus is assigned to a longitudinal surface mode. In the theoretical calculations of Ref. 17 no surface mode or resonance has been identified (see Figs. 12 and 13 of Ref. 17) which can be attributed to this observed mode. Since it is not always easy to identify surface resonances from slab calculations it is still possible that such a mode exists for the interatomic interaction model used in the calculations.

In interpreting these experiments, it is important to realize that the scattering signal contains nearly equal contributions from the KF as well as from the MnF_2 surfaces (see Sec. II). Since no broadening of the Rayleigh mode is observed within the experimental error of ≈ 0.2 meV it appears that the Rayleigh modes of both surfaces either have almost exactly the same dispersion curves or the intensity of one of them is much smaller than the other. The lowering of the Rayleigh mode with respect to the bulk band edge is about 7%. This is comparable with the lowering of the Rayleigh mode in the alkali halides.⁴⁶ For example, in KF at the \bar{M} point theory predicts that the Rayleigh mode is 11% below the transverse bulk band edge.^{47,48}

The $\langle 110 \rangle$ azimuthal direction is more interesting because of the phase transition and the appearance of superstructure peaks. A series of TOF spectra at 280 K and appropriate scan curves are shown in Fig. 15. The predominant inelastic peak in all of the spectra is assigned to the Rayleigh mode. A second mode at slightly higher phonon energies is well resolved at the energy loss side of the spectra and attributed to a longitudinal mode. In addition, between the diffuse elastic peak and the Rayleigh energy loss peak a broad maximum indicated by an S is observed at $\theta_i = 35^\circ$ and 34° . The data obtained in this direction at 320 and 280 K were identical and both are presented in Fig. 16 together with the theoretical predicted surface modes and some of the bulk bands. Up to $Q \leq 0.8 \text{ \AA}^{-1}$ the lower-lying experimental data points follow essentially the $\Sigma_4(\text{TA})$ bulk band edge. At larger Q

values the intensity of this mode decreases rapidly and it becomes undetectable. There it becomes a resonance and because of mixing with bulk modes its amplitude at the surface is greatly reduced.

The additional experimental points 2 meV above the Rayleigh mode in the Q interval between 0.3 and 0.5 \AA^{-1} can be assigned to a longitudinal surface mode peeled off from the Σ_1 longitudinal acoustic bulk band. A few very weak points were observed in the first part of the Brillouin zone in the vicinity of the Σ_3 optical bulk band edge. The small discrepancy in the theoretical Rayleigh mode, which lies below the experimental points in the first part of the Brillouin zone is perhaps not so surprising, since the interaction model used in the calculations is a central force shell model, which cannot reproduce the large violation of the Cauchy relations in KMnF_3 and therefore does not precisely fit the velocity of sound in

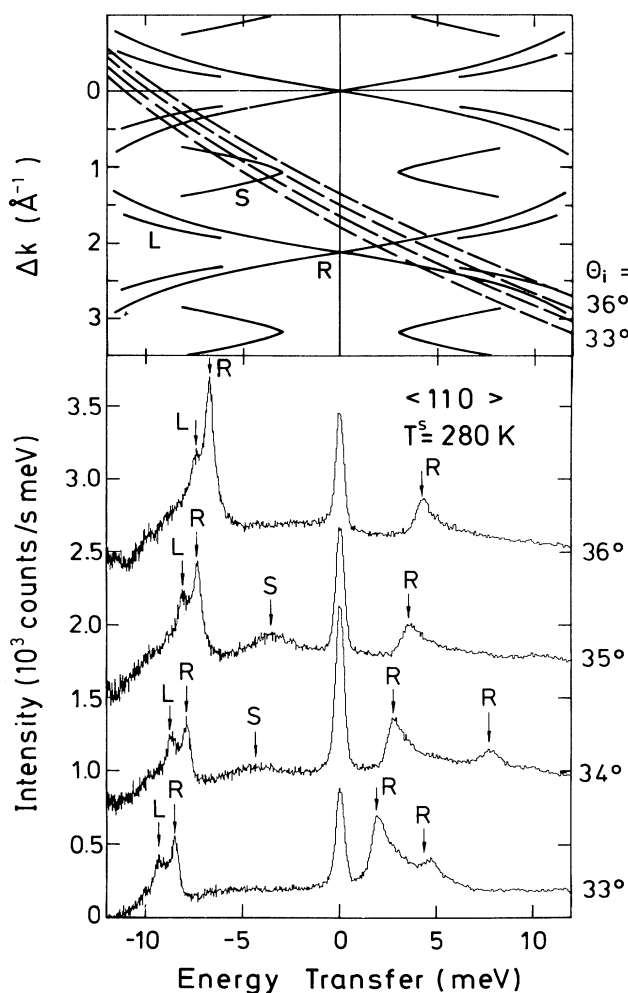


FIG. 15. Series of TOF spectra converted to an energy transfer scale in the $\langle 110 \rangle$ direction at $T^s = 280$ K at various incident angles. The corresponding scan curves and the experimental dispersion curves are plotted on the top. $k_i = 6.03 \text{ \AA}^{-1}$. The phonon peaks are labeled as R for the Rayleigh mode, L for the longitudinal mode, and S for the "soft mode" close to \bar{M} .

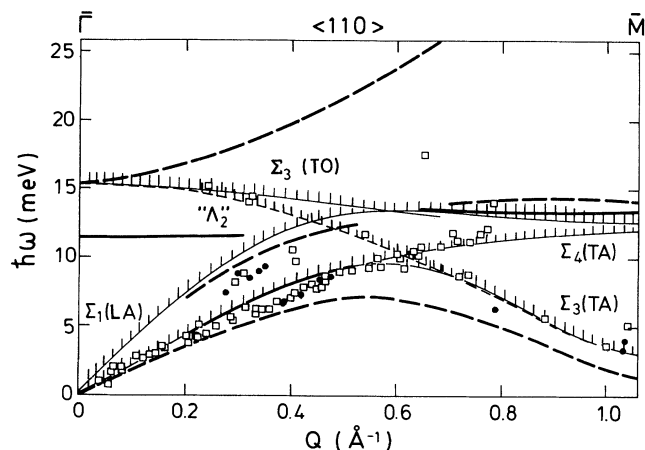


FIG. 16. Comparison of experimental and theoretical dispersion curves in surface phonon energy $\hbar\omega$ vs wave vector Q plot in the $\langle 110 \rangle$ direction in the high temperature phase. The meaning of the hatched, solid, and dashed curves is the same as in Fig. 14. The dashed boundary indicates the projected band edge of the Λ_2 bulk mode in the $\langle 111 \rangle$ direction. The squares denote measurements at $T^s = 320$ K and $k_i = 6.05 \text{ \AA}^{-1}$ and solid circles, measurements at $T^s = 280$ K and $k_i = 6.03 \text{ \AA}^{-1}$.

the bulk.

The lowest energy transfer experimental data points, indicated with an R in Fig. 15, lie just below the $\Sigma_4(\text{TA})$ band edge and then become a resonance at wave vectors larger than $Q > 0.8 \text{ \AA}^{-1}$ while the predicted Rayleigh mode for surface I, indicated as a dashed curve in Fig. 16, bends off to lower energies even below the lowest bulk band. The weak broad points at low energy transfer in Fig. 15 are close to this bulk band edge, but lie above the predicted Rayleigh mode for surface I. In the following we want to explain why the intensities of the experimental data points for the mode indicated by an S in this Q -vector region are so weak and why the experimental observed mode indicated by R in Fig. 15 seems to cross the S mode in Fig. 15. We discuss whether the observed S mode is a surface mode of surface I or surface II or neither of those but only the bulk band edge.

The observed surface mode indicated by an S can originate from the $\Sigma_3(\text{TA})$ band edge as well as from the edge of the Λ_2 bulk mode in the $\langle 111 \rangle$ direction projected onto the (001) surface plane, shown in Fig. 16 as a dashed boundary. In the former case the surface mode has SH polarization. For simple crystals it is impossible to excite such an SH mode with HAS in the sagittal plane scattering geometry because the polarization vector has no component in the direction of the surface normal and is perpendicular to the Q vector. For more complicated crystals like KMnF_3 this is no longer strictly true. A group-theoretical analysis⁴⁹ shows that for the $\Sigma_3(\text{TA})$ mode the displacement of the atoms in the surface I (KF) are strictly perpendicular to the wave vector and the surface normal but the displacements of the atoms in the surface II may have also longitudinal components. Therefore this

mode can only be seen from surface II. In principle pure longitudinal modes are accessible to HAS but with much smaller cross sections than modes with polarization perpendicular to the surface.⁵⁰ Therefore this mode would produce only a weak peak in the HAS TOF spectra.

However, because of the strong softening of the longitudinal optical bulk Λ_2 mode the corresponding projected bulk band edge extends to very low energies for wave vectors in the second half of the Brillouin zone. In that region the band edge coincides nearly with the Σ_3 transverse band edge shown in Fig. 16. The Λ_2 mode is two-fold degenerate and the projection of this band onto the surface plane has a SH polarized as well as a SP polarized part. At the \bar{M} point the SP polarized part of this bulk band has only longitudinal components for surface I and therefore has only a small HAS cross section.

For atoms of surface II the polarization vector of the SP polarized part as well as the SH polarized part of the projected Λ_2 bulk band have components perpendicular to the surface which is the preferred polarization for HAS. However, the calculations of Reiger *et al.*¹⁷ do not predict a surface localized mode for this surface. A weak localization at the surface implies a small vibration amplitude of the atoms of the topmost layer resulting in a small inelastic cross section for this mode.

The above considerations show that in any of the discussed cases only a weak scattering intensity is expected for the S mode in agreement with the experimental result. However, we cannot decide which surface contributes more to this branch. While the modes for surface II possess the preferred polarization the theory predicts higher localization for the surface I. We cannot rule out that we simply observe the bulk band edge for surface II.

The $\Sigma_4(\text{TA})$ mode has a vertical polarization and the surface mode originating from this band gives rise to strong phonon intensities in the HAS spectra. At $Q \approx 0.6 \text{ \AA}^{-1}$ the projection of this band on the surface crosses the projection of the Λ_2 mode which has an SP as well as an SH polarized part. Therefore the corresponding SP polarized surface mode (Rayleigh mode) changes its character and bends over to the soft mode originating from the projected Λ_2 band. However no gap in the crossing region could be observed. The assignment of the experimentally observed S mode to the Rayleigh mode is consistent with symmetry considerations discussed above, but contributions from the SH polarized surface mode are also possible in which case the two surface modes can cross each other. The two contributions cannot be separated in our experiment due to resolution limitations. However, the gap, i.e., the energy distance of the Rayleigh mode to the bulk band edge at $Q \approx 0.6 \text{ \AA}^{-1}$ must be smaller than 1 meV.

As in the $\langle 100 \rangle$ direction no significant broadening of the experimental Rayleigh mode is observed indicating either that this mode has the same energy in both surfaces or that the cross section is much smaller for one of the two surfaces. No significant experimental evidence is found for the predicted resonance at 11.5 meV near $\bar{\Gamma}$ for surface II. We have also tried to find higher optical modes by using higher incident beam energy up to ≈ 60 meV. However, with increasing incident energy the mul-

tiphonon background increases rapidly and apparently masks any additional single phonon peaks.

B. Phonon dispersion curves in the low temperature phase and the temperature dependence of the Rayleigh mode

In the $\langle 100 \rangle$ direction there are no significant changes in the phonon spectra between the low temperature phase and the high temperature phase. Figure 13 reveals no significant differences in the TOF spectra compared to that of the high temperature phase as discussed earlier. In the low temperature phase the area of the Brillouin zone is halved because of the $\sqrt{2} \times \sqrt{2} R 45^\circ$ superstructure. Some additional backfolded surface modes such as the Lucas mode are predicted by the theory¹⁸ since the \overline{MX} direction is mapped onto the $\overline{\Gamma X}$ direction. However, in the low energy region accessible to HAS no additional phonon modes with high intensity are expected.

In the $\langle 110 \rangle$ direction the \overline{M} point is folded back onto the $\overline{\Gamma}$ point. Figure 17 shows a series of TOF spectra in the low temperature phase at $T^s = 170$ K. As in the other direction no additional modes were observed in the experiment except some weak structures at $\approx +10$ meV (indicated by arrows in Fig. 17) close to $\overline{\Gamma}$ as can be seen by comparing Fig. 17 with Fig. 15. However, this mode cannot be assigned unambiguously to a backfolded mode. This mode could be due to the 11.5-meV mode of surface II already predicted for the high temperature phase near

the $\overline{\Gamma}$ point. Possibly it has been observed in the low temperature phase because of the temperature-induced increase of the single phonon intensities. The only other major changes are the increases in intensity relative to the other phonon peaks of the broad part of the Rayleigh mode (S mode).

In the simple picture of a pure soft-mode-induced phase transition the soft mode is expected to go to zero energy at the phase transition temperature. At lower temperatures the energy of this mode increases again and in addition at \overline{M} which is the new $\overline{\Gamma}'$ point of the reconstructed surface at low temperatures a new Rayleigh mode originates from the superstructure peak at $\overline{\Gamma}'$. In the case of KMnF_3 the energy of the soft phonon does not go to zero because of the weak first-order character of the transition but qualitatively the same behavior is expected. The intensity of the new Rayleigh mode is then expected to be superimposed on top of the "soft phonon" mode of the high temperature phase. Although possibly present it was not possible to resolve these two components. Even at 125 K the width of these broad peaks remains essentially unchanged.

However, a true softening of the Rayleigh mode in the high temperature phase is observed as can be seen from Fig. 18. TOF spectra are plotted with decreasing temperature from the top to the bottom. Whereas at an incident angle of 35° the mode is visible at all temperatures, at 36° , where the scan curve is closer to the \overline{M} point at zero energy loss, this mode becomes only visible in Fig. 18 at temperatures of 170 and 220 K. At 220 K the temperature is well above the transition temperature so that no backfolded Rayleigh mode exists. The position of the "soft phonon" peak does not change with temperature at 35° . This is explained by the fact that this peak actually consists of two unresolved peaks of the same branch with positive and negative phonon wave vectors. The scan curve cuts the branches at different energies and therefore masks almost all of the temperature dependence of the low energy part.

The question whether the soft phonon originates from the surface I or from surface II cannot be answered unequivocally by our measurements as discussed above. The assumption that the observed soft mode is due to scattering from surface II would remove the discrepancy for this mode between theory and experiment because then we simply observe more or less the bulk band edge of the Σ_3 mode rather than the true Rayleigh mode which exists only at surface I in this region. But the authors of Ref. 17 expected a much higher transition temperature of $T_c^s = 214$ K than actually observed. A correction for the observed transition temperature would shift the Rayleigh mode more toward the bulk band edge close to \overline{M} and bring the results closer into agreement even if the experimental soft mode is mainly due to surface I.⁵¹

Figure 19 shows the experimental dispersion curves below the phase transition. Because of the higher phonon intensity the surface resonance which follows the $\Sigma_4(\text{TA})$ bulk band edge is observable up to \overline{M} . As in the high temperature phase all observed modes presumably have sagittal plane polarization. Therefore the surface modes cannot cross each other. However, a gap in the

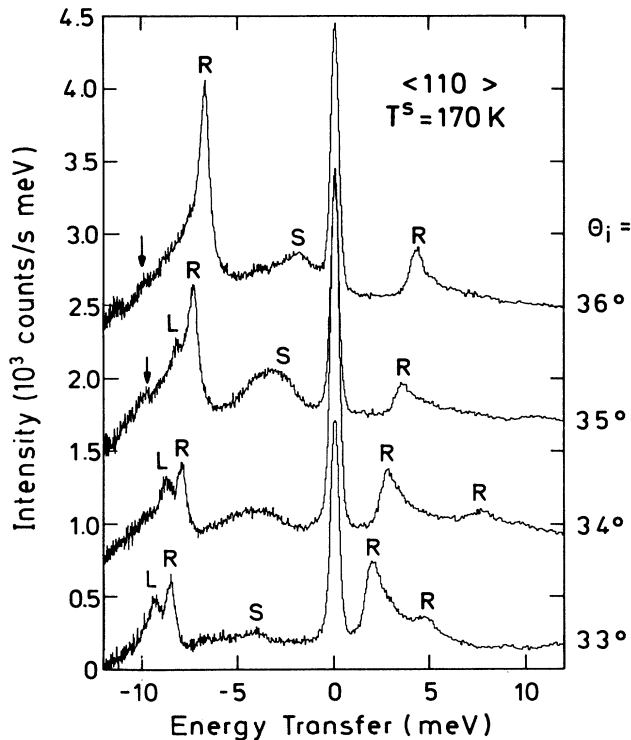


FIG. 17. Same as Fig. 15 but at $T^s = 170$ K. In the low temperature phase an additional very weak mode can be resolved indicated by arrows in the TOF spectra.

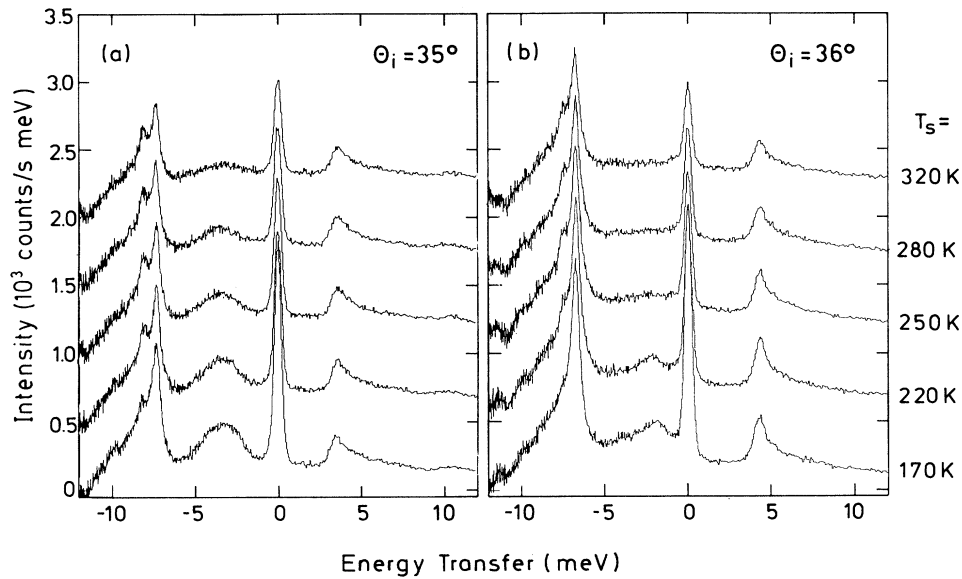


FIG. 18. Series of TOF spectra converted to an energy transfer scale at (a) $\theta_i = 35^\circ$ and (b) $\theta_i = 36^\circ$ with surface temperatures between $T^s = 320$ and 170 K. The $\theta_i = 36^\circ$ measurements scan through the \bar{M} point at a lower absolute energy transfer than the measurements at $\theta_i = 35^\circ$. The measured transition temperature at the surface is $T_c^s = 191$ K.

crossing region at $Q \approx 0.6 \text{ \AA}^{-1}$ is not resolved. The slope of the Rayleigh mode at the \bar{M} point (the new $\bar{\Gamma}'$ point) is much different from that at $\bar{\Gamma}$ indicating that the backfolded Rayleigh mode is not dominant. In Fig. 19 the slope of the Rayleigh mode is indicated by dashed lines. We found no hints for backfolded modes in the whole ΔK space.

V. THERMAL INSTABILITY OF THE SURFACE AT HIGHER TEMPERATURES

As shown in Sec. II the crystal surface has a large amount of structural defects immediately after cleavage,

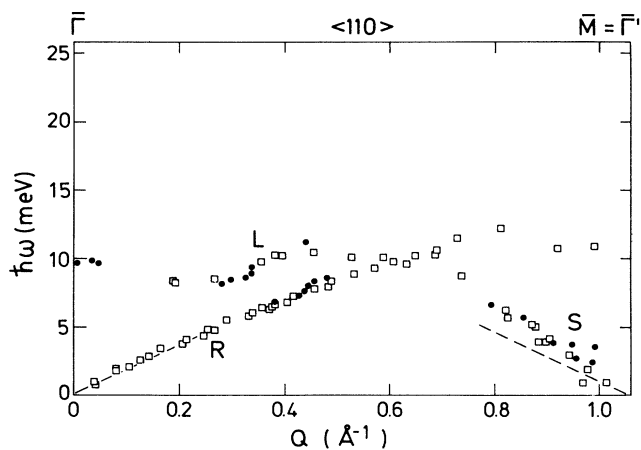


FIG. 19. Comparison of experimental and theoretical dispersion curves in a surface phonon energy $\hbar\omega$ vs wave vector Q plot for the $\langle 110 \rangle$ direction in the low temperature phase. Open squares denote measurements at $T^s = 125$ K, solid circles at $T^s = 170$ K. The slope of the Rayleigh mode is indicated by dashed lines originating from $\bar{\Gamma}$ and at \bar{M} , the new $\bar{\Gamma}'$ point.

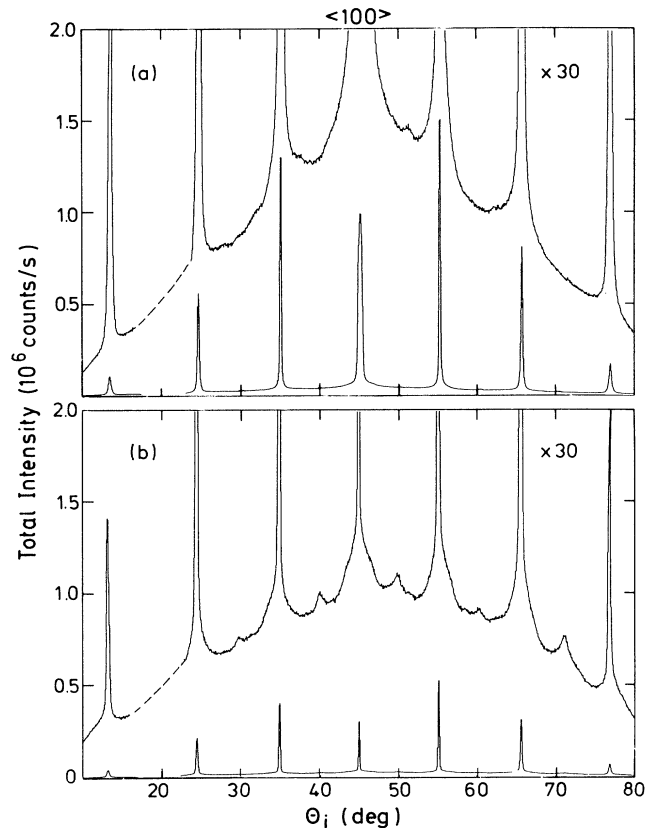


FIG. 20. Angular distributions in the $\langle 100 \rangle$ direction at $T^s = 320$ K and $k_i = 6.03 \text{ \AA}^{-1}$, (a) the crystal was never heated above $T^s = 320$ K after cleavage, (b) after the crystal was heated to $T^s = 487$ K. In the magnified scale additional half-order peaks are visible. Note that this direction is different from that on which the 191-K phase transition induced superstructure occurs.

as indicated by broad satellites on the specular and the diffraction peaks in the $\langle 110 \rangle$ direction. These satellites disappear partially after several days at 320 K and after a few hours at 340 K. In all measurements discussed above the crystal was never heated beyond 340 K. When however the crystal was heated to higher temperatures the intensity of the diffraction peak decreased drastically by more than an order of magnitude. This is shown in Fig. 20 where the angular distributions at 320 K in the $\langle 100 \rangle$ direction are plotted in (a) before heating and in (b) after heating the crystal to 487 K which is well below the melting point at $T=1286$ K.⁵² While the defect induced broadening of the specular peak vanished after heating, the change in the shape of the background indicates an increase of the diffuse elastic component of the intensity as was confirmed by TOF measurements. In the total angular distribution of the heated crystal shown in Fig. 20(b) a weak superstructure of double lattice spacing was observed. Note that this direction is different from that on which the 191-K phase transition occurs. An angular distribution of only the elastic component reveals that these additional peaks are due to elastic scattering and therefore are related to a structural change. This superstructure however only appears to be an intermediate state since after a second heating to ≈ 500 K it disappears again. No sharp threshold temperature could be identified for the onset of this disordered state of the surface.

In Fig. 21 the specular intensity is plotted versus the surface temperature. The intensity decreases initially exponential up to 380 K but then the slope decreases until at about 420 K the intensity drops very rapidly. On cooling of the crystal the intensity recovers partially but the slope is smaller than the initial slope on the heating cycle. The lowest curve was measured after changing the nozzle some days after the upper two measurements. Therefore

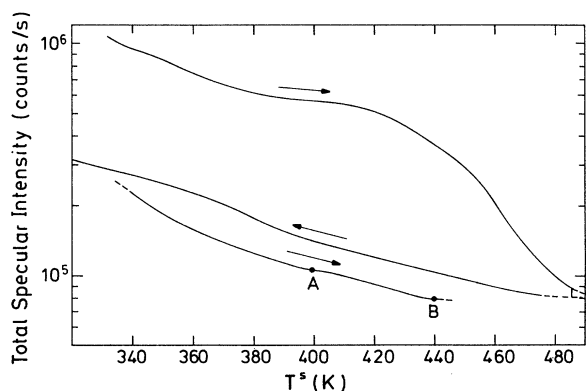


FIG. 21. Specular intensity vs crystal temperature in the $\langle 100 \rangle$ direction at $k_i = 6.03 \text{ \AA}^{-1}$. The crystal was first heated to $T^s = 487$ K at a rate of 0.01 K/sec (uppermost curve) and subsequently cooled at 0.008 K/sec. During a second heating of the crystal (lowest curve) the temperature was held constant at points A and B for approximately 2 hr. No change of the intensity was observed indicating that mass transport on the crystal surface was in equilibrium during the heating of the crystal.

the absolute intensities are not fully comparable. The slope of the curve is unchanged with respect to the second curve indicating a nearly reversible change of the intensity on the second heating. In all case the temperature was changed very slowly (about 0.01 K/sec), so that it would appear reasonable to assume that the curves are measured under conditions of thermodynamic equilibrium at each time. At the points A and B the temperature was held constant about 2 h for each point. No further decrease of the intensity was observed in either case.

The mechanism of this irreversible change of the surface structure remains unclear. We cannot decide whether atoms evaporate from the surface or the surface becomes partially disordered due to diffusion processes at the surface. The alkali halide (001) surfaces are not known to exhibit a thermally induced surface disorder at temperatures far below their melting points. At not too high temperatures only molecules at step edges evaporate, which does not lead to an increase in the surface disorder. For NaCl, which has a bulk melting point of 1073 K evaporation from step edges occur at temperatures higher than 450 K.⁵³ But even at 720 K the average step distance is of the order of 1000 \AA , which is larger than the transfer width of our HAS instrument. On the other hand very recent measurements in our group give some hints, that thermal-induced irreversible surface disorder may also occur on the MgO(001) surface. For the $\text{KMnF}_3(001)$ surface the behavior of the specular intensity versus the incident wave vector indicates that the surface that had been heated above $T \approx 480$ K has many terraces separated by large step heights as shown in Fig. 22. The fast oscillations of about 0.2 \AA^{-1} correspond to the interference between areas with a height difference of five lattice constants.

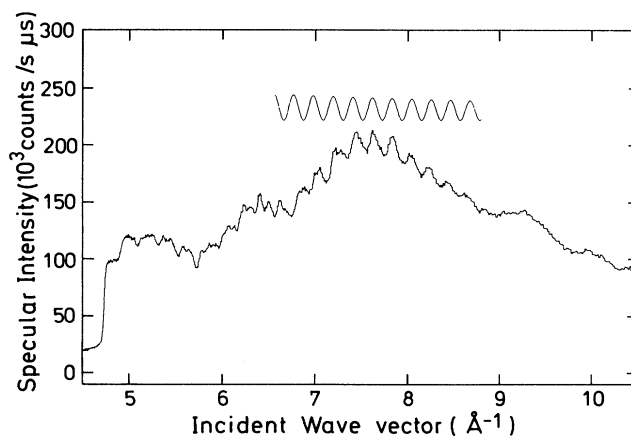


FIG. 22. Specular intensity vs incident wave vector measured at $T^s = 320$ K after the crystal had been heated to $T^s = 487$ K. The fast oscillations of about 0.2 \AA^{-1} are induced by the interference between adjacent terraces with a difference in height of about five double layers ($5 \times 4.19 \text{ \AA}$). The solid curve shown for comparison is the result of a simulation with this step height.

VI. CONCLUSION

The present measurements are the first detailed structural and dynamical investigations on a pristine undisturbed in-vacuum cleaved perovskite surface. Recently Bickel *et al.*¹⁵ reported extensive detailed LEED structural observation on the SrTiO₃(001) surface which had been prepared by an elaborate *in situ* preparation procedure. Their procedure which is similar to that used to prepare metal surfaces consisted in alternate cycles of sputtering and subsequent annealing in hydrogen and oxygen. It is known that such a process can lead to changes in the stoichiometry and structure at the surface and even in the bulk.^{9,26} For KMnF₃ which is generally thought to be more stable than SrTiO₃ our experiments reveal that even a rather moderate heating of the crystal can lead to drastic changes in the surface structure. Thus we feel that in future work on perovskites extreme care must be used to assure an undisturbed ideal surface. Moreover because of the extreme sensitivity of these surfaces it would appear that helium atom scattering is the preferred diffraction technique. As opposed to electron scattering it is entirely nondestructive and compared to electrons and x rays only sensitive to the outermost surface layer.

The temperature dependence of the measured diffraction peak intensities reveals a surface phase transition at $T_c^s = 191$ K at which the surface reconstructs to a $c(2 \times 2)$ superstructure. The measured transition temperature T_c^s lies above the highest reported value for the bulk transition T_c^b . But since we were not able to measure the bulk and the surface transition simultaneously we cannot, in view of the reported small differences in T_c^b for different samples, completely rule out that T_c^b equals T_c^s . The critical exponent $\beta_1 = 0.63 \pm 0.03$ derived from the superstructure peak intensities are considerably higher than the bulk value of $\beta = 0.2857 \pm 0.0006$ but this is predicted if either $T_c^s > T_c^b$ or $T_c^s = T_c^b$. Assuming an ordinary phase transition, a value of $\beta_1 \approx 0.67$ can be estimated from theoretical values for the Heisenberg model and the experimental bulk value for β_b which is in reasonable agreement with our experimental result on β_1 . However, if a surface transition exists it may be difficult to derive a reliable value for β_1 because of the small difference in temperature for T_c^s and T_c^b . A combined HAS x-ray diffraction experiment would be desirable to clarify the question if a surface transition exists or not.

The experimental observed surface phonon dispersion curves agree with the predictions of Reiger *et al.*¹⁷ within the experimental accuracy and the limitations of the model used in their calculations. At room temperature the experimental energy of the Rayleigh mode at the \bar{M} point lies below the calculated value. This is consistent with the smaller value of the experimental T_c^s compared to the theoretical value. Taking into account the true T_c^s in the calculation the energy of this mode would shift in the right direction. Since up to now almost no surface phonon with a pure longitudinal polarization has been observed, it would appear most likely that the observed intensity close to the bulk band edge of the Σ_3 mode is due to scattering from surface II. There are

several other minor differences between experiment and theory. For one the energy of the optical surface mode along the $\langle 100 \rangle$ direction near $\bar{\Gamma}$ lies below the calculated value by about 2 meV. Moreover the theory does not predict the observed longitudinal resonance in the $\langle 110 \rangle$ direction. A direct comparison of the measured phonon intensities with calculations would be desirable. Such calculations are straightforward if the polarization vectors of the individual modes are known. Unfortunately they were not reported in the publication of Reiger *et al.*¹⁷

The present helium atom scattering experiments also provide new information on the concentration and structure of defects on the surface. The cleaved surface shows much greater concentrations of defects compared to the alkali halide surfaces. Most of the defects disappear at room temperature after several days. However, after heating the crystal to temperature higher than 420 K the difference intensities decrease almost entirely irreversibly. The diffuse elastic intensity due to defects is increased strongly after heating the crystal to ≈ 480 K and the one phonon peaks disappear in the TOF spectra, indicating a large amount of disorder of the surface. This disorder could be identified as due to the creation of many terraces separated by steps. The difference in height of these terraces is up to five double layers within the transfer width

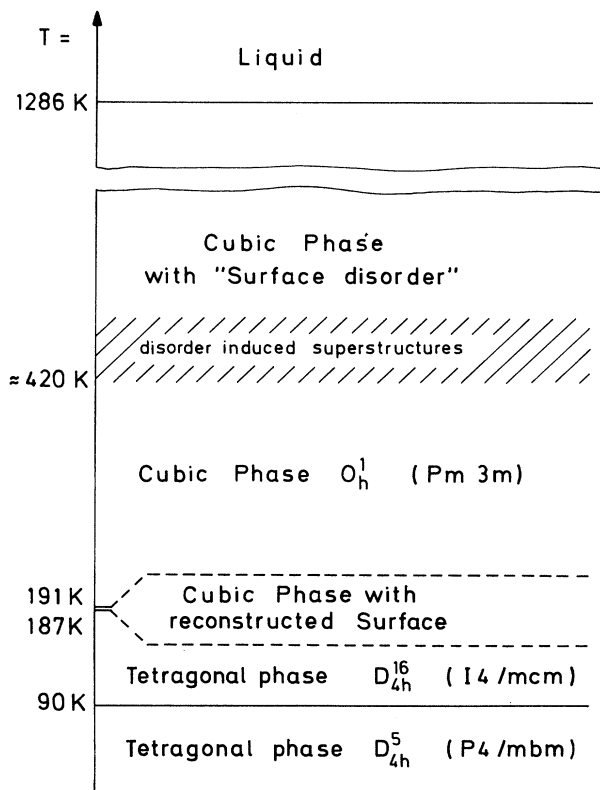


FIG. 23. Proposed phase diagram of the KMnF₃(001) surface. The present work covers the temperature range from ≈ 140 K to ≈ 500 K.

of the apparatus. The mechanism of this change of the surface is not yet fully understood. Since the changes are irreversible and persist after cooling at room temperature they can be studied by microscopic real space techniques such as atomic force microscopy (AFM) or perhaps electron microscopy gold decoration techniques.⁵⁴

The structural phases of the $\text{KMnF}_3(001)$ surface are summarized in the proposed phase digram shown in Fig. 23. Besides the three bulk structural phases (with space groups O_h^1 , D_{4h}^{16} , and D_{4h}^5 , respectively⁵) the slightly higher measured phase transition temperature $T_c^s = 191$ K at the surface compared to the bulk transition temperature $T_c^b = 187.5$ K may indicate an additional surface localized phase. At temperatures higher than ≈ 420 K, which is far below the melting point of 1286 K, the surface becomes gradually disordered.

ACKNOWLEDGMENTS

We want to thank especially Dr. R. C. C. Ward (Oxford, U.K.) for providing the excellent KMnF_3 single crystals which made this experiment possible. We gratefully acknowledge stimulating discussions with Dr. J. Prade and Professor U. Schröder (both from Regensburg, Germany) and Professor J. Skofronick (Tallahassee, Florida). The authors thank Dr. D. M. Smilgies for reading the manuscript and many helpful discussions.

APPENDIX

It is demonstrated in the following that in the distorted wave Born approximation (DWBA) the intensity of the scattered atoms at the superstructure peak is proportional to the square of the order parameter η .

The interaction potential in the low temperature phase can be written as

$$V_i = \sum_l \sum_\kappa \sum_j v_\kappa(\mathbf{r} - \mathbf{r}_{l\kappa j} + \mathbf{u}_{l\kappa j}), \quad (\text{A1})$$

where $v_\kappa(\mathbf{r})$ is the pair potential between the He atom and the κ th type of atoms in the crystal where $\mathbf{r}_{l\kappa j} = (\mathbf{R}_{l\kappa j}, z_{l\kappa j})$ is the position of the $(l\kappa j)$ th atom. $l = (L, l_z)$ runs over all lattice sites, j over all equivalent atoms in the high temperature phase, and κ over all inequivalent atoms of the unit cell. $\mathbf{u}_{l\kappa j}$ is the displacement of the atom with respect to the thermally averaged position $\mathbf{r}_{l\kappa j}$. $\mathbf{r}_{l\kappa j}$ consists of two parts, one describing the average position of the $(l\kappa j)$ th atom in the high temperature phase, $\mathbf{r}_{l\kappa j}^0$ and the other the static displacement $\mathbf{u}_{l\kappa j}^{\text{stat}}$ from that position in the low temperature phase:

$$\mathbf{r}_{l\kappa j} = \mathbf{r}_{l\kappa j}^0 + \mathbf{u}_{l\kappa j}^{\text{stat}}. \quad (\text{A2})$$

$\mathbf{r}_{l\kappa j}^0$ can be further split up into the location of the origin of the l th unit cell and the relative position of the (κj) th atom in that unit cell:

$$\mathbf{r}_{l\kappa j}^0 = \mathbf{r}_l^0 + \mathbf{r}_{\kappa j}^0. \quad (\text{A3})$$

$\mathbf{u}_{l\kappa j}^{\text{stat}}$ can be expressed as

$$\mathbf{u}_{l\kappa j}^{\text{stat}} = \eta \exp(i\mathbf{Q} \cdot \mathbf{R}_{L\kappa j})(\mathbf{e}_{l_z \kappa \parallel}, \mathbf{e}_{l_z \kappa \perp}) + \text{c.c.}, \quad (\text{A4})$$

where η is the order parameter, $\mathbf{e}_{l_z \kappa} = (\mathbf{e}_{l_z \kappa \parallel}, \mathbf{e}_{l_z \kappa \perp})$ the polarization vector of the soft mode with wave vector \mathbf{Q} , which induces the phase transition, and $\mathbf{e}_{l_z \kappa \parallel}$ and $\mathbf{e}_{l_z \kappa \perp}$ are the parallel and perpendicular components of the polarization vector. c.c. denotes the conjugated complex of the preceding term. Within the DWBA the differential cross section can be written⁴³

$$\frac{d\sigma}{d\Omega} = \frac{2\pi m^2 |\mathbf{k}_f|}{\hbar^4 k_{iz}} \sum_G |\langle \chi(k_{fz}; z) U_G(z) \chi(k_{iz}; z) \rangle|^2 \delta(\mathbf{K}_f - \mathbf{K}_i - \mathbf{G}), \quad (\text{A5})$$

where k_{iz} and k_{fz} are the z component of the incoming and outgoing wave vectors, respectively, m is the mass of the He atom, $\chi(k_{iz}; z)$ and $\chi(k_{fz}; z)$ the z -dependent parts of the wave function for the lateral and thermal averaged potential V_i . The sum runs over all surface reciprocal lattice vectors of the superstructure. The Fourier transform interaction potential U_G is given by

$$\begin{aligned} U_G &= \sum_{l_z} \sum_\kappa \sum_j \int dk_z \exp(ik_z z) \exp[-i(\mathbf{G}, k_z) \cdot (\mathbf{r}_{j\kappa}^0 + \mathbf{u}_{l\kappa j}^{\text{stat}})] \exp[-W_{l_z}^{\kappa j}(\mathbf{G}, k_z)] v_{\mathbf{G}k_z}^\kappa \\ &= \sum_{l_z} \sum_\kappa \sum_j \int dk_z \exp[ik_z(z - z_{l_z \kappa}^0)] \exp(-i\mathbf{G} \cdot \mathbf{R}_{j\kappa}^0) \Phi_j \exp[-W_{l_z}^{\kappa j}(\mathbf{G}, k_z)] v_{\mathbf{G}k_z}^\kappa, \end{aligned} \quad (\text{A6})$$

with

$$\Phi_j = \exp[i\eta \mathbf{G} \cdot \mathbf{e}_{l_z \kappa \parallel}] \exp(-i\mathbf{Q} \cdot \mathbf{R}_{j\kappa}^0) + i\eta k_z \mathbf{e}_{l_z \kappa \perp} \exp(-i\mathbf{Q} \cdot \mathbf{R}_{j\kappa}^0) + \text{c.c.}, \quad (\text{A7})$$

where $W_{l_z}^{\kappa j}(\mathbf{G}, k_z)$ is the Debye-Waller factor of the $(l_z \kappa j)$ th atom in the unit cell and $v_{\mathbf{G}k_z}^\kappa$ is the Fourier transform of the pair potential $v_\kappa(\mathbf{r})$. The phase factor Φ_j contains all the information on the order parameter η . Since η is small compared to the lattice vector, Φ_j can be expanded

$$\begin{aligned} \exp(-i\mathbf{G}\cdot\mathbf{R}_{j\kappa}^0)\Phi_j = & \exp(-i\mathbf{G}\cdot\mathbf{R}_{j\kappa}^0) + \eta\{\exp[-i(\mathbf{G}-\mathbf{Q})\cdot\mathbf{R}_{j\kappa}^0](i\mathbf{G}\cdot\mathbf{e}_{l_z\kappa\parallel} + ik_z e_{l_z\kappa\perp}) \\ & - \exp[-i(\mathbf{G}+\mathbf{Q})\cdot\mathbf{R}_{j\kappa}^0](i\mathbf{G}\cdot\bar{\mathbf{e}}_{l_z\kappa\parallel} + ik_z \bar{e}_{l_z\kappa\perp})\} + O(\eta^2). \end{aligned} \quad (\text{A8})$$

For small η it is expected that the Debye-Waller factor does not depend on j so that in Eq. (A6) the sum over j can be factored out. If \mathbf{G} also happens to be a Bragg peak \mathbf{G}' of the high temperature phase then $\sum_j \exp(-i\mathbf{G}\cdot\mathbf{R}_{j\kappa}^0) = M$, the quotient of the unit cell area of the low temperature phase and the normal phase. If on the other hand \mathbf{G} is a first-order superstructure peak ($\mathbf{G} = \mathbf{G}' \pm \mathbf{Q}$) then $\sum_j \exp(-i\mathbf{G}\cdot\mathbf{R}_{j\kappa}^0) = 0$ and $\sum_j \exp[-i(\mathbf{G} \pm \mathbf{Q})\cdot\mathbf{R}_{j\kappa}^0] = M$. Therefore, the differential cross section at a superstructure peak $\mathbf{G} = \mathbf{G}' + \mathbf{Q}$ is given by

$$\frac{d\sigma}{d\Omega} = \eta^2 \frac{2\pi m^2 |\mathbf{k}_f|}{\hbar^4 k_{iz}} |\langle \chi(k_{fz}; z) \tilde{U}_{\mathbf{G}}(z) \chi(k_{fz}; z) \rangle|^2, \quad (\text{A9})$$

with

$$\tilde{U}_{\mathbf{G}}(z) = M \sum_{l_z} \sum_{\kappa} \int dk_z \exp[ik_z(z - z_{l_z\kappa}^0)] \exp[-W_{l_z}^{\kappa}(\mathbf{G}, k_z)] v_{\mathbf{G}k_z}^{\kappa} (i\mathbf{G}\cdot\mathbf{e}_{l_z\kappa\parallel} + k_z e_{l_z\kappa\perp}). \quad (\text{A10})$$

The matrix element in Eq. (A9) does not depend on the order parameter η . Therefore the differential cross section is directly proportional to the square of η . For a superstructure peak with $\mathbf{G} = \mathbf{G}' - \mathbf{Q}$ the last term in Eq. (A10) has to be replaced by its conjugated complex value. In principle Eq. (A10) cannot be solved analytically since

the Debye-Waller term cannot be factored out of the matrix element because of its k_z dependence. But it has been shown experimentally that in most cases the temperature of the Bragg peaks far away from any phase transition can be described by the simple exponential Debye-Waller factor.

¹A. D. Bruce and R. A. Cowley, *Adv. Phys.* **29**, 219 (1980).

²K. A. Müller, in *Nonlinear Phenomena at Phase Transitions and Instabilities*, edited by T. Riste (Plenum, New York, 1982).

³G. Shirane, V. J. Minciewicz, and A. Linz, *Solid State Commun.* **8**, 1941 (1970).

⁴U. J. Nicholls and R. A. Cowley, *J. Phys. C* **20**, 3417 (1987).

⁵M. Hidaka, *J. Phys. Soc. Jpn.* **39**, 180 (1975).

⁶M. Hidaka, H. Fujii, and S. Maeda, *Phase Transitions* **6**, 101 (1986).

⁷S. M. Shapiro, J. D. Axe, G. Shirane, and T. Riste, *Phys. Rev. B* **6**, 4332 (1972).

⁸J. Töpler, B. Alefeld, and A. Heidemann, *J. Phys. C* **10**, 635 (1977).

⁹C. N. W. Darlington and D. A. O'Connor, *J. Phys. C* **9**, 3561 (1976).

¹⁰R. Silbergliitt, *Solid State Commun.* **11**, 247 (1972).

¹¹A. D. Bruce, K. A. Müller, and W. Berlinger, *Phys. Rev. Lett.* **42**, 185 (1979).

¹²B. I. Halperin and C. M. Varma, *Phys. Rev. B* **14**, 4030 (1976).

¹³S. R. Andrews, *Phase Transitions* **11**, 181 (1988).

¹⁴A. Gibaud, H. You, S. Shapiro, and J. Y. Gesland, *Phys. Rev. B* **42**, 8255 (1990).

¹⁵N. Bickel, G. Schmidt, K. Heinz, and K. Müller, *Phys. Rev. Lett.* **62**, 2009 (1989).

¹⁶J. Prade, U. Schröder, F. W. de Wette, A. D. Kulkarni, and W. Kress, *Phys. Rev. B* (to be published).

¹⁷R. Reiger, J. Prade, U. Schröder, W. Kress, F. W. de Wette, and A. D. Kulkarni, *Phys. Rev. B* **39**, 7938 (1989).

¹⁸J. Prade, A. D. Kulkarni, F. W. de Wette, R. Reiger, U. Schröder, and W. Kress, *Surf. Sci.* **211/212**, 329 (1989).

¹⁹J. P. Toennies, *J. Vac. Sci. Technol.* **A5**, 440 (1986); **A2**, 1055 (1984).

²⁰J. P. Toennies, in *Solvay Conference on Surface Science Invited*

Lectures and Discussions, Vol. 14 of Springer Series of Surface Science, edited by F. W. de Wette (Springer-Verlag, Berlin, 1988), p. 248.

²¹A. M. Lahee, J. R. Manson, J. P. Toennies, and Ch. Wöll, *J. Chem. Phys.* **86**, 7194 (1987).

²²G. Brusdeylins, R. B. Doak, and J. P. Toennies, *Phys. Rev. B* **27**, 3662 (1983).

²³D. M. Smilgies and J. P. Toennies, *Rev. Sci. Instrum.* **59**, 2185 (1988).

²⁴R. Vollmer (unpublished).

²⁵V. E. Henrich, G. Dresselhaus, and H. J. Zeiger, *Phys. Rev. B* **17**, 4908 (1978).

²⁶J. E. T. Anderson and P. J. Møller, *Appl. Phys. Lett.* **56**, 1847 (1990).

²⁷R. C. C. Ward, University of Oxford, Department of Physics, Clarendon Laboratory, Park Road, Oxford, OX1 3PV, U.K.

²⁸P. Poelsema, S. T. de Zwart, and G. Comsa, *Phys. Rev. B* **49**, 578 (1982); P. Poelsema and G. Comsa, *Scattering of Thermal Energy Atoms*, Vol. 115, Springer Tracts of Modern Physics (Springer, Berlin, 1989).

²⁹J. Hinch, A. Lock, and J. P. Toennies, G. Zhang, *J. Vac. Sci. Technol.* **B7**, 1260 (1989).

³⁰J. Lapujoulade, *Surf. Sci.* **108**, 317 (1981).

³¹A. Okazaki and Y. Suemune, *J. Phys. Soc. Jpn.* **16**, 671 (1961).

³²N. Esbjerg and J. K. Nørskov, *Phys. Rev. Lett.* **45**, 807 (1980).

³³V. Celli, D. Eichenauer, A. Kaufhold, and J. P. Toennies, *J. Chem. Phys.* **83**, 2504 (1985).

³⁴J. Wollschläger, J. Falta, and M. Henzler, *Appl. Phys. A* **50**, 57 (1990).

³⁵G. Benedek, G. Brusdeylins, J. P. Toennies, and R. B. Doak, *Phys. Rev. B* **27**, 2488 (1983).

³⁶U. Cox, A. Gibaud, and R. A. Cowley, *Phys. Rev. Lett.* **61**, 982 (1988); A. Gibaud, R. A. Cowley, and J. Novet, *Phase Transitions* **14**, 129 (1989).

- ³⁷K. Binder, in *Phase Transitions and Critical Phenomena*, edited by C. Domb and J. L. Lebowitz (Academic, New York, 1983), Vol. 8.
- ³⁸L. D. Landau and E. M. Lifschitz, *Lehrbuch der Theoretischen Physik*, Bd. 5, edited by P. Ziesche (Akademie Verlag, Berlin, 1981).
- ³⁹A. D. Bruce, *Adv. Phys.* **29**, 111 (1980).
- ⁴⁰J. C. Leguillou and J. Zinn-Justin, *Phys. Rev. B* **21**, 3976 (1980).
- ⁴¹K. Binder, *Thin Solid Films* **20**, 367 (1974).
- ⁴²H. W. Diehl and S. Dietrich, *Z. Phys. B* **42**, 65 (1981).
- ⁴³R. Manson and V. Celli, *Surf. Sci.* **24**, 495 (1971).
- ⁴⁴H. Sakashita, N. Ohama, and A. Okazaki, *J. Phys. Soc. Jpn.* **50**, 4013 (1981).
- ⁴⁵K. Gesi, J. D. Axe, G. Shirane, and A. Linz, *Phys. Rev. B* **5**, 1933 (1972).
- ⁴⁶J. P. Toennies, in *Dynamics of Gas-Surface Interaction*, edited by G. Benedek and U. Valbusa (Springer, Berlin, 1982).
- ⁴⁷W. Kress, F. W. de Wette, A. D. Kulkarni, and U. Schröder, *Phys. Rev. B* **35**, 5783 (1987).
- ⁴⁸H. Bilz and W. Kress, in *Phonon Dispersion Relations in Insulators*, edited by M. Cardona, P. Fulde, and H.-J. Queisser (Springer, Berlin, 1979).
- ⁴⁹R. A. Cowley, *Phys. Rev.* **134**, A981 (1964).
- ⁵⁰V. Bortolani, A. Francini, N. Garcia, F. Nizzoli, and G. Santoro, *Phys. Rev. Lett.* **52**, 429 (1984).
- ⁵¹U. Schröder, private communication.
- ⁵²*Crystal Structure Data of Inorganic Compounds*, Vol. III/7a of Landolt-Börnstein, edited by K.-H. Hellwege and A. M. Hellwege (Springer, Berlin, 1973), p. 269.
- ⁵³H. Höche, *Solid State Phenomena* **12**, 87 (1990).
- ⁵⁴H. Höche (private communication).